*sustainability*

MDPI

*Article*

# Unravelling the Natural and Anthropogenic Controls on Karst Groundwater Hydrochemistry in the Zaozhuang Area, Northern China: A Combined Hydrogeochemical and PMF Source Apportionment Study

**Bo Li [1,2], Caiping Hu [1,2], Zhizheng Liu [3], Shuai Gao [1,2], Ziqi Wei [4], Yue Wei [1,2], Binglin Jiang [1,2], Ke Liu [1,2] and Hongyan An [4,5,*]**

[1] Shandong Provincial Geo-Mineral Engineering Exploration Institute (801 Institute of Hydrogeology and Engineering Geology), Shandong Provincial Bureau of Geology & Mineral Resources, Jinan 250014, China; libosddk801@163.com (B.L.)
[2] Shandong Engineering Research Center for Environmental Protection and Remediation on Groundwater, Jinan 250014, China
[3] Shandong Institute of Geological Survey, Jinan 250014, China
[4] Langfang Integrated Natural Resources Survey Center, China Geological Survey, Tianjin 300304, China
[5] Innovation Base for Natural Resources Monitoring Technology in the Lower Reaches of Yongding River, Geological Society of China, Langfang 065000, China
* Correspondence: anhongyan9485@126.com

## Abstract

Karst groundwater is the principal water supply for Zaozhuang City and an essential safeguard for the local environment. In May 2025, 131 karst groundwater samples were collected and analysed using Piper, Durov, and Gibbs diagrams; ion ratios; mineral saturation indices; and multivariate statistics, and the sources of the dissolved constituents were quantified with positive matrix factorisation (PMF). The water is weakly alkaline, with pH between 7.04 and 7.78 (mean 7.33) and total dissolved solids (TDSs) between 288 and 2578 mg/L (mean 609.10 mg/L). $HCO_3^-$ and $Ca^{2+}$ are the dominant ions, and the water is mainly of the $HCO_3^-$Ca type. Rock weathering and mineral dissolution, together with anthropogenic inputs, control the water chemistry: $Ca^{2+}$, $Mg^{2+}$ and $HCO_3^-$ are derived mainly from carbonate weathering and dissolution, $SO_4^{2-}$ from the dissolution of sulfate minerals such as gypsum, $Na^+$, $K^+$ and $Cl^-$ from evaporite dissolution and anthropogenic inputs, and $NO_3^-$ mainly from agricultural activities; cation exchange modifies the ionic balance but does not add solute mass. The PMF model resolves four sources—carbonate weathering, agricultural nitrogen input, sulfate mineral dissolution, and halite dissolution together with anthropogenic salt input—which account for 36.85%, 27.41%, 24.81% and 10.92% of the solute mass, respectively. Carbonate weathering supplies most of the $HCO_3^-$ and $Mg^{2+}$, the agricultural nitrogen factor accounts for 95.62% of the $NO_3^-$, sulfate mineral dissolution for 83.92% of the $SO_4^{2-}$, and the halite–anthropogenic salt factor for 71.32% of the $Na^+$ and 43.89% of the $Cl^-$. Mineral dissolution and water–rock interaction are the main sources of the solutes, while agricultural nitrogen and salt input are the principal anthropogenic contributions. Carbonate and sulfate mineral dissolution together carry about 62% of the solute mass and agricultural nitrogen and salt input about 38%, so the protection of this aquifer should focus on nitrate from farming and salt and sulfate inputs in the urban and mining districts.

**Keywords:** karst groundwater; hydrochemical characteristics; water–rock interaction; controlling factors; positive matrix factorization (PMF); Zaozhuang City

Check for updates

Academic Editor: Fernando António Leal Pacheco

Received: 7 September 2026
Revised: 21 October 2026
Accepted: 22 October 2026
Published: 24 October 2026

**Copyright:** © 2026 by the authors. Licensee MDPI, Basel, Switzerland. This article is an open access article distributed under the terms and conditions of the Creative Commons Attribution (CC BY) license.

## 1. Introduction

Karst groundwater is a vital freshwater resource in many parts of the world and, in northern China in particular, it plays an irreplaceable role in sustaining ecosystems and local economies [1,2]. In karst aquifers, water is stored mainly in dissolution fissures, dissolution pores and caves. Because the rock mass is highly heterogeneous and the system is relatively open, groundwater moves quickly, its chemistry responds rapidly to both natural and anthropogenic forcing, and it evolves in a complex manner [1–3]. Understanding the chemical characteristics of karst groundwater and the factors that control them is therefore important for water supply, water quality protection and the conservation of karst ecosystems [4,5].

The chemical composition of groundwater is governed by several processes acting simultaneously, including water–rock interaction, rainfall recharge, evaporation and anthropogenic inputs [4,6,7]. In karst regions, carbonate rock dissolution is the dominant natural process, and it generally makes $Ca^{2+}$, $Mg^{2+}$ and $HCO_3^-$ the dominant ions in the water [4–6]. Sulfate minerals such as gypsum also dissolve, and external acids (sulfuric and nitric) participate in carbonate dissolution, releasing additional $SO_4^{2-}$ and other species [4,8]. The sulfuric acid is generated mainly by the oxidation of pyrite and other sulfide minerals, which occur as accessory phases in the coal measures and locally in the carbonate rocks; the nitric acid is generated mainly by the nitrification of fertiliser and manure nitrogen in the soil zone. Evaporite minerals such as halite contribute $Na^+$ and $Cl^-$; the weathering of silicates releases $Na^+$, $K^+$, and dissolved silica but supplies only a minor part of the solute mass in a carbonate terrain; and anthropogenic inputs add further $NO_3^-$, $Cl^-$, and $SO_4^{2-}$ through fertiliser, manure, sewage, mining, and industrial salt [1,2,9,10]. Cation exchange and evaporation further modify the ion balance and direction of chemical evolution [4,7]. In recent decades, fertiliser application, coal mining and domestic sewage have released large amounts of $NO_3^-$, $Cl^-$ and $SO_4^{2-}$ into karst aquifers, altering both the chemistry and the quality of the water; anthropogenic forcing is now a leading driver of karst groundwater evolution [1,2,9,10].

Two groups of anthropogenic sources are distinguished in this paper. Farming denotes the application of chemical fertilisers, including nitrogen, compound, and sulfate-bearing fertilisers such as ammonium sulfate and single superphosphate; the spreading of manure and of sewage sludge used as fertiliser; the irrigation of cropland with wastewater; and aquaculture, which discharges feed residues and excreta into the rivers and canals that recharge the aquifer. Mining denotes coal mining in the Carboniferous–Permian coal measures of the Zaozhuang basin: mine drainage, coal-washing effluent, leachate from coal waste piles and the dewatering of workings release sulfate, chloride and sodium, and abandoned shafts, adits and collapse columns connect the mined seams with the overlying karst aquifer. Because the coal measures lie below the karst aquifer that supplies the wells, sulfate of mining origin can reach the wells only along these pathways or where mine water is discharged at the surface, and sulfate also enters the soil as a fertiliser amendment and with irrigation water, so that a sulfate-rich sample does not by itself identify a geological source.

Various tools are used to characterise groundwater chemistry and identify the sources of the dissolved ions, the most common being the Piper, Durov, and Gibbs diagrams; ion ratios; and multivariate statistics [2,5,11]. The Gibbs diagram provides a qualitative indication of the relative importance of precipitation, rock weathering and evaporation [11]. Ion ratios help to trace individual ions and the water–rock processes involved [4]; however, no single ratio is a unique diagnostic of one process because different processes can produce

the same value, and the ratios are therefore interpreted here together with the multivariate source apportionment. Most of these tools are nevertheless qualitative or only semi-quantitative, and they cannot quantify the contribution of each source. Receptor models were introduced into groundwater research to fill this gap, and positive matrix factorisation (PMF) is one of the most widely used. PMF was first developed for source apportionment of airborne particulate matter and has since been applied to water quality studies [12–20]. It weights every measurement by its own uncertainty and constrains the factor profiles and factor contributions to be non-negative [19–21], and it has been applied successfully to karst groundwater in a number of recent studies [15,22–26].

Karst is well developed in central-southern Shandong (the Luzhongnan area), where karst groundwater supplies cities such as Jinan, Tai'an, Zibo and Zaozhuang, and its chemistry, evolution and controlling factors have been studied extensively [27]. Song Yinsheng [28] provided the first comprehensive overview of the large karst springs of this region. Xu Huizhen et al. [29] and Zhang Ya et al. [7] used hydrochemistry and isotopes to trace groundwater evolution in the Jinan spring catchment. Meng Linghua [30] and Li Xiaobo et al. [9] investigated recharge sources and sulfate sources in the Tai'an urban area, and Teng Yue et al. [31] characterised the chemistry and controls of karst water in the Zihe River basin. Zhao Qingling et al. [32] examined the chemical origin of the Shuangcun karst water system. These studies provide a solid basis for the region, but most of them focused on a single spring catchment or river basin, and research on Zaozhuang City, an important karst water supply area, remains limited. In particular, no previous study has apportioned the solutes of this area with a receptor model that carries the measurement uncertainty of every sample; to our knowledge, this is the first PMF apportionment of karst groundwater in the Luzhongnan area. Beyond the apportionment itself, the approach shows how much solute mass is carried by each of the processes identified from the ion ratios and saturation indices.

Against this background, the present study focuses on the karst groundwater of Zaozhuang City. A total of 131 karst water samples were collected and analysed using the Piper, Durov, and Gibbs diagrams; ion ratios; mineral saturation indices; and multivariate statistics, with the aim of characterising the water chemistry and sources of its ions. PMF was then applied to quantify the contributions of carbonate weathering, agricultural nitrogen input, sulfate mineral dissolution and halite dissolution together with anthropogenic salt input. Because the survey reported here is a single campaign, the seasonal behaviour of the nitrate and sulfate loads is not known, and a routine monitoring network is needed before the apportionment can be used to test the effect of management measures; the design of such a network is therefore also considered. The results provide a basis for the sustainable use, quality protection and pollution control of karst groundwater in Zaozhuang City.

## 2. Materials and Methods

### *2.1. Overview of the Study Area*

The study area lies in southern Shandong Province (116°48′–117°49′ E, 34°27′–35°19′ N) and covers the whole of Zaozhuang City, which administers the Shizhong, Xuecheng, Yicheng, Tai'erzhuang and Shanting Districts together with Tengzhou City, a total of 4564 km$^2$ (Figure 1). The area forms part of the low mountains and hills of central-southern Shandong and of the Huang-Huai alluvial plain. The topography descends from northeast to southwest, with the highest point (620.4 m) in Shanting District and the lowest (about 24.5 m) beside the lakeshore in the west and the Grand Canal in the south. Low mountains and hills dominate the landscape, followed by alluvial–proluvial plains and depressions. The area belongs to the canal system of the Huaihe River basin and is bounded by Weishan Lake to the west. It contains 24 rivers of various sizes, and the Zaozhuang section of the

Beijing–Hangzhou Grand Canal crosses the south of the city for 39 km. The main rivers (the Yijia, Yicheng Dasha, Chengguo and Panlong Rivers) all rise in the northeastern mountains and are mostly rain-fed seasonal streams. The climate is warm temperate, semi-humid and monsoonal, with four distinct seasons; the multi-year mean temperature is 13.2–14.2 °C, the mean annual precipitation is about 800 mm and the frost-free period lasts 190–215 days. Rainfall is the main source of groundwater recharge [28,32].

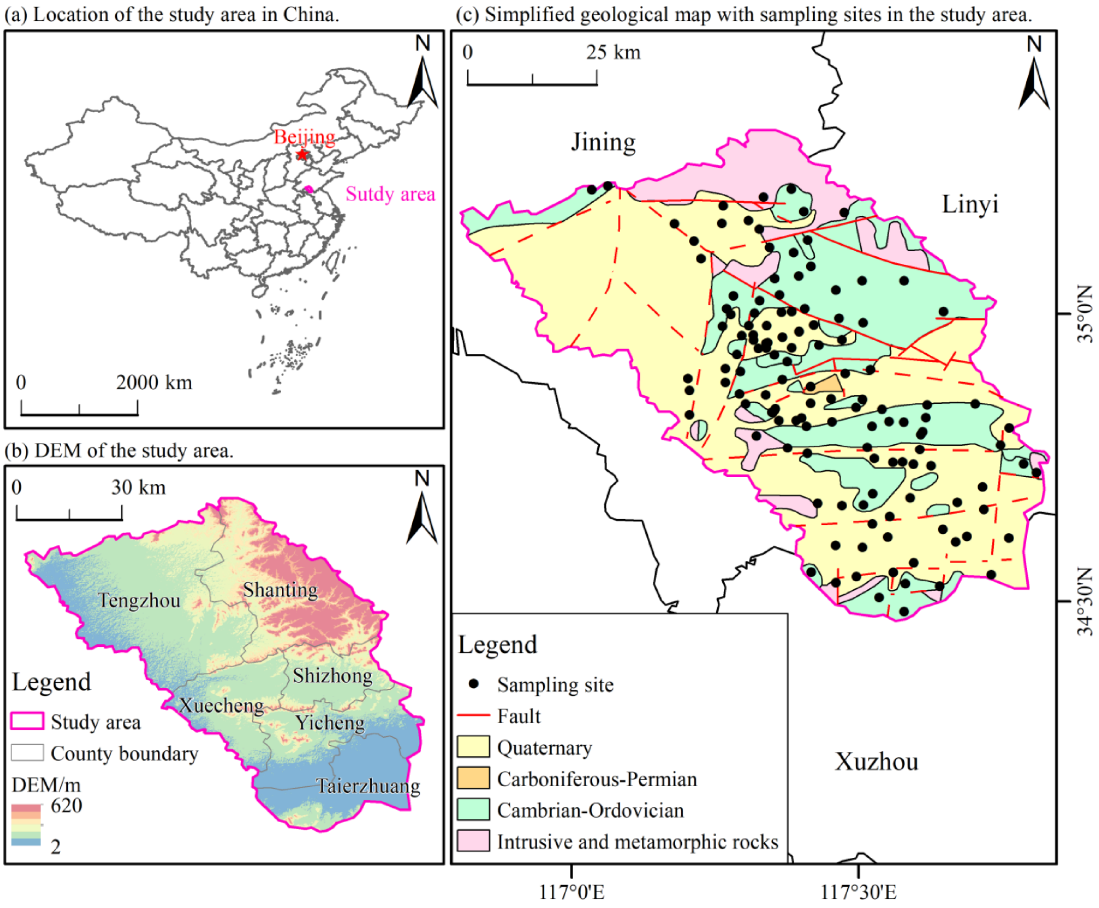



**Figure 1.** Location of the study area and distribution of sampling sites: (**a**) location of the study area in China; (**b**) digital elevation model (DEM) of the study area; (**c**) simplified geological map of the study area with the sampling sites. In (**b**), the elevation ranges from 2 to 620 m. In (**c**), the solid red lines are faults, the dashed red lines are buried (inferred) faults, the pink line is the boundary of the study area and the black dots are the sampling sites.

Tectonically, the study area lies in the Luzhong uplift of the Luxi block of the North China Plate. The regional structure is complex and dominated by faults, with folds of secondary importance. Two sets of structures, trending nearly E-W and nearly N-S, cut through the area. The nearly E-W faults are the Zaozhuang, Caowangmu, Yixian and Hantai Faults, and the nearly N-S faults are the Yishan and Huashigou Faults; folds such as the Zaozhuang syncline also occur, and together they form the present structural framework [28,32]. Stratigraphically, the area belongs to the North China region. It exposes Archean rocks; Cambrian, Ordovician, Carboniferous and Permian strata of the Palaeozoic and Quaternary deposits of the Cenozoic, whereas the Upper Ordovician, Devonian, Lower Carboniferous and Triassic are absent. Carbonate rocks are widespread and consist mainly of limestone, dolomitic limestone, dolomite and argillaceous dolomite, cropping out mostly in the northeast, centre and south of the area. The Ordovician limestone occupies the intermountain basins; it is pure, brittle and thick, with well-developed karst.

Karstification is strongest in the Lower Ordovician dolomitic limestone and the thick-bedded limestone of the Middle Ordovician Majiagou Formation. The Cambrian Mantou and Zhangxia Formations crop out in the northern and central mountains, where karst is unevenly developed. Carboniferous–Permian coal-bearing strata are concealed within the Zaozhuang basin.

On the basis of the lithology of the aquifer groups and the nature of the water-storage voids, the groundwater can be divided into four types: karst fissure water in carbonate rocks, pore water in unconsolidated sediments, pore-fissure water in clastic rocks and fissure water in igneous and metamorphic rocks. The karst fissure water in carbonate rocks is the focus of this study [28,32]. It occurs mainly in the karst fissures of the Ordovician and Cambrian limestones, and its aquifers are chiefly the limestone and dolomite of the Ordovician Majiagou Formation and the Cambrian Sanshanzi Formation of the Jiulong Group, which are mostly exposed or semi-exposed. The karst takes the form of dissolution fissures, honeycomb dissolution and caves, and the water yield is high, so that this aquifer is the main source of groundwater supply in the area. Pore water in unconsolidated sediments occurs in the Tengxi Plain, the Zaonan Plain and the intermountain basins, where the Quaternary is generally 20–40 m thick and consists mainly of medium-coarse sand, silty clay and sandy gravel with a moderate to strong water yield. Pore-fissure water in clastic rocks occurs in the interlayer fissures of the Carboniferous–Permian strata and has a rather poor yield, and fissure water in igneous and metamorphic rocks occurs in the weathering and structural fissures of the metamorphic and intrusive rocks in the north and centre, with a weak yield. Groundwater is recharged mainly by rainfall, with a minor contribution from surface water leakage. It flows generally from north to south and from west to east and drains south-eastwards after converging. Discharge is dominated by pumping at centralised supply sources such as the Shiliquan, Dingzhuang–Dongwangzhuang and Kekou well fields, followed by spring discharge and runoff.

### *2.2. Sample Collection and Laboratory Analysis*

Sampling points were distributed according to the hydrogeological zoning and the occurrence of karst water in the area. In May 2025, 131 karst groundwater samples were collected from drinking water supply wells and karst springs (129 wells and 2 springs); most of the sampling points tap confined karst water of the Cambrian–Ordovician carbonate aquifer (126 samples) and one taps unconfined water. The sampling density is one sample per 34.8 $km^2$ over the 4564 $km^2$ study area. The depth of individual wells was not recorded in the survey, but all sampling points are completed in the same Cambrian–Ordovician karst horizon. Before sampling, each well was pumped until the water represented the aquifer; the samples were then sealed, kept in the dark and delivered to the laboratory without delay.

Field parameters—pH, water temperature, electrical conductivity (EC), redox potential (Eh) and dissolved oxygen (DO)—were measured in situ with a portable multi-parameter meter. Water temperature ranged from 10.9 to 24.5 °C (mean 17.1 °C), EC from 425 to 2030 μS/cm (mean 746.2 μS/cm) and pH from 7.04 to 7.78 (mean 7.33). The cations $K^+$, $Na^+$, $Ca^{2+}$ and $Mg^{2+}$ were determined by inductively coupled plasma optical emission spectrometry (ICP-OES) and the anions $Cl^-$, $SO_4^{2-}$, $NO_3^-$, $F^-$ and $I^-$ by ion chromatography (IC). $HCO_3^-$ was determined by acid titration and TDS and total hardness by the gravimetric method and EDTA complexometric titration, respectively. Trace constituents ($H_2SiO_3$, $NH_4^+$, COD, Mn, Al, Cd, Cu and Zn) were determined by the corresponding national standard methods. Nitrite and dissolved silica are also available: $NO_2^-$ ranges from 0.004 to 1.28 mg/L (median 0.005 mg/L, with only one sample above 1 mg/L) and $H_2SiO_3$ from 9.8 to 46.0 mg/L (mean 15.9 mg/L); both are used below as supporting

evidence for the nitrogen inputs and silicate weathering. All analyses were performed by the laboratory of the Shandong Provincial Geo-mineral Engineering Exploration Institute, which is qualified for this work. The charge balance was checked for every sample: the charge balance error, CBE = (sum of cations − sum of anions)/(sum of cations + sum of anions) × 100%, ranges from −4.23% to +2.87%, with a mean of −0.83% and a median of −1.21%, and all 131 samples fall within ±5%, which confirms the reliability of the data.

### *2.3. Data Processing Methods*

ArcGIS (v.3.7.1) was used to map the study area and sampling sites, and the spatial distributions of the chemical components were interpolated by inverse distance weighting (IDW). The Piper, Durov, and Gibbs diagrams; ion ratio plots; ion end-member diagram; and mineral saturation index plots were produced with Origin [11]. SPSS (v.32.0.0) was used for the descriptive statistics and correlation analysis. Source apportionment was carried out with positive matrix factorisation (PMF), a weighted least-squares receptor model [19,20]. PMF expresses the measured concentration matrix X as the product of a factor contribution matrix G and a factor profile matrix F, X = GF + E, where E is the residual matrix. Both G and F are constrained to be non-negative, and the solution is obtained by minimising the weighted sum of squared residuals $Q = \Sigma_i\Sigma_j[(x_{ij} - \Sigma_k g_{ik}f_{kj})/u_{ij}]^2$, in which $u_{ij}$ is the uncertainty of the measurement $x_{ij}$ [19–21].

The ten ions $K^+$, $Na^+$, $Ca^{2+}$, $Mg^{2+}$, $Cl^-$, $SO_4^{2-}$, $NO_3^-$, $HCO_3^-$, $F^-$ and $I^-$ were used as model inputs, the same set as in the hydrochemical analysis; pH was not used as a model species because it is a master variable of the carbonate system rather than a conservative solute. Each element of X requires a paired uncertainty, which was constructed following the protocol of the US EPA PMF 5.0 model [20]. For a species with method detection limit MDL, $u_{ij} = [(EF \cdot x_{ij})^2 + (0.5 \cdot MDL)^2]^{0.5}$ when $x_{ij} > MDL$, whereas values at or below the MDL were replaced by MDL/2 and assigned $u_{ij} = 5/6 \cdot MDL$. The error fraction EF was set to 0.10, which covers the analytical precision of ICP-OES and IC together with the uncertainty of sampling, and an additional modelling uncertainty EMU of 30% was applied, $u_{ij} = (u_{ij}^2 + (EMU \cdot x_{ij})^2)^{0.5}$, to account for the part of the variability that a finite number of factors cannot reproduce [20]. The method detection limits were 0.05 mg/L for $K^+$, $Na^+$, $Mg^{2+}$, and $F^-$; 0.10 mg/L for $Ca^{2+}$, $Cl^-$, and $NO_3^-$; 0.50 mg/L for $SO_4^{2-}$; 1.00 mg/L for $HCO_3^-$; and 0.003 mg/L for $I^-$.

Each species was screened with its signal-to-noise ratio S/N [20,33]. All ten species had S/N above 1 and were retained. Iodide lay at or below its detection limit in 22 of the 131 samples, and fluoride was present at low concentrations close to its own limit, so both were classified as 'Weak' species and their uncertainties were multiplied by three [20,33]. Solutions with two to eight factors were computed, and for each solution, the objective function was minimised from 80 random and singular-vector-based starting points, with the run with the lowest Q being retained. The four-factor solution was selected on the basis of $Q/Q_{exp}$ (1.17) and the hydrogeochemical interpretability of the factors. Here, $Q_{exp} = mn - p(m + n) = 746$ was the Q value expected for 131 samples, 10 species and 4 factors when the uncertainties were correct [20]. The solution was then refined with a bounded quasi-Newton step, and PMF was run in robust mode, so that a point with $|e_{ij}/u_{ij}| > 4$ received a reduced weight [21].

The uncertainty of the final solution was estimated in two ways. First, 200 bootstrap runs were performed by resampling the samples with replacement; the factors of each run were matched to those of the base run by correlation, and the 5th and 95th percentiles of the contributions were taken as the confidence interval [34]. Second, the rotational freedom of the solution was explored by rotating every pair of factors through angles of up to 45°; the reported solution was unique within $\Delta Q \leq 5\%$ of the base Q [20]. For every

ion, the measured and modelled concentrations were compared through the coefficient ofdetermination $R^2$.

Mineral saturation indices were computed with PHREEQC 3 [35], using the default phreeqc.dat thermodynamic database, the Debye–Hückel activity model and the measured in situ water temperature of each sample (10.9–24.5 °C); the input species were $Ca^{2+}$, $Mg^{2+}$, $Na^+$, $K^+$, $HCO_3^-$, $SO_4^{2-}$, $Cl^-$, $NO_3^-$, $F^-$ and $SiO_2$. The saturation index (SI) is a standard measure in hydrogeochemistry that indicates the state in which the chemical components occur, and it is widely used to establish whether a mineral is dissolving or precipitating [36]. It is defined as SI = log(IAP/K), where IAP is the ion activity product of the dissolution reaction and K is the equilibrium constant at the given temperature. A value of SI = 0 indicates equilibrium, SI > 0 oversaturation with a tendency to precipitate and SI < 0 undersaturation with a tendency to dissolve. The SI values of calcite, dolomite, gypsum and aragonite were computed here in order to assess the dissolution–precipitation state of the carbonate and sulfate mineral end-members in the groundwater.

## 3. Results and Discussion

### *3.1. Hydrochemical Characteristics of Karst Groundwater*

Table 1 summarises the statistics of the hydrochemical parameters and Figure 2 shows the range of each parameter. The pH of the karst water ranges from 7.04 to 7.78 (mean 7.33, standard deviation 0.16, coefficient of variation 2.13%), so the water is weakly alkaline and chemically stable, with only small spatial differences. TDS ranges from 288 to 2578 mg/L (mean 609.10 mg/L, median 532 mg/L); its maximum is about nine times its minimum, and its CV reaches 45.58%. The salinity of the karst water is therefore relatively high and clearly variable in space, which may reflect the aquifer lithology, the runoff conditions and anthropogenic inputs [37].

**Table 1.** Descriptive statistics of hydrochemical parameters for karst groundwater in the study area. Concentrations are in mg/L, pH is dimensionless and CV is the coefficient of variation (%).

| Variable | pH | TDS | $K^+$ | $Na^+$ | $Ca^{2+}$ | $Mg^{2+}$ | $Cl^-$ | $SO_4^{2-}$ | $NO_3^-$ | $HCO_3^-$ | $F^-$ | $I^-$ |
|---|---|---|---|---|---|---|---|---|---|---|---|---|
| Min | 7.04 | 288.00 | 0.10 | 3.31 | 39.90 | 5.46 | 6.91 | 19.80 | 2.64 | 63.00 | 0.10 | 0.003 |
| Max | 7.78 | 2578.00 | 10.40 | 178.40 | 704.00 | 62.80 | 250.00 | 1545.00 | 278.00 | 422.00 | 1.61 | 0.16 |
| Mean | 7.33 | 609.10 | 0.99 | 27.95 | 142.08 | 23.16 | 47.22 | 151.39 | 69.39 | 293.47 | 0.49 | 0.031 |
| SD | 0.16 | 277.61 | 1.17 | 28.71 | 66.62 | 11.61 | 40.56 | 175.90 | 45.95 | 56.85 | 0.31 | 0.024 |
| CV | 2.13 | 45.58 | 117.75 | 102.72 | 46.89 | 50.12 | 85.91 | 116.19 | 66.22 | 19.37 | 63.22 | 77.19 |

In the karst water of the study area, $Ca^{2+}$ is the dominant cation (mean 142.08 mg/L), followed by $Na^+$ (27.95 mg/L) and $Mg^{2+}$ (23.16 mg/L), with $K^+$ the least abundant (0.99 mg/L); the order is $Ca^{2+} > Na^+ > Mg^{2+} > K^+$. Among the anions, $HCO_3^-$ is dominant (mean 293.47 mg/L), followed by $SO_4^{2-}$ (151.39 mg/L), $NO_3^-$ (69.39 mg/L) and $Cl^-$ (47.22 mg/L), in the order $HCO_3^- > SO_4^{2-} > NO_3^- > Cl^-$. The water is mainly of the $HCO_3^-$Ca type, which reflects the control exerted by carbonate dissolution and aquifer lithology. The mean $NO_3^-$ concentration of 69.39 mg/L is distinctly high, and several samples exceed the drinking water limit, which shows that inputs from agriculture and other anthropogenic sources have reached the karst aquifer. The concentrations of $F^-$ and $I^-$ are low, with means of 0.49 mg/L and 0.031 mg/L, respectively.

The coefficients of variation of $K^+$ (117.75%), $SO_4^{2-}$ (116.19%) and $Na^+$ (102.72%) exceed 100%, indicating very strong spatial variation and marked local differences in contaminant input or the intensity of water–rock reaction. $Cl^-$ (85.91%), $I^-$ (77.19%), $NO_3^-$ (66.22%), $F^-$ (63.22%), $Mg^{2+}$ (50.12%) and $Ca^{2+}$ (46.89%) have CVs between 45% and 90%, which indicates moderate spatial variation, whereas TDS (45.58%) and $HCO_3^-$ (19.37%)

are fairly evenly distributed; pH has the lowest CV of all (2.13%). Because every well is completed in the same Cambrian–Ordovician horizon, this spread cannot be ascribed to differences in sampling depth; it reflects instead the heterogeneous distribution of point sources (fertiliser, manure, sewage and mine water) and the strong local variation of the aquifer materials, in particular the clay-rich interbeds that control exchange and the gypsum-bearing beds that control sulfate.

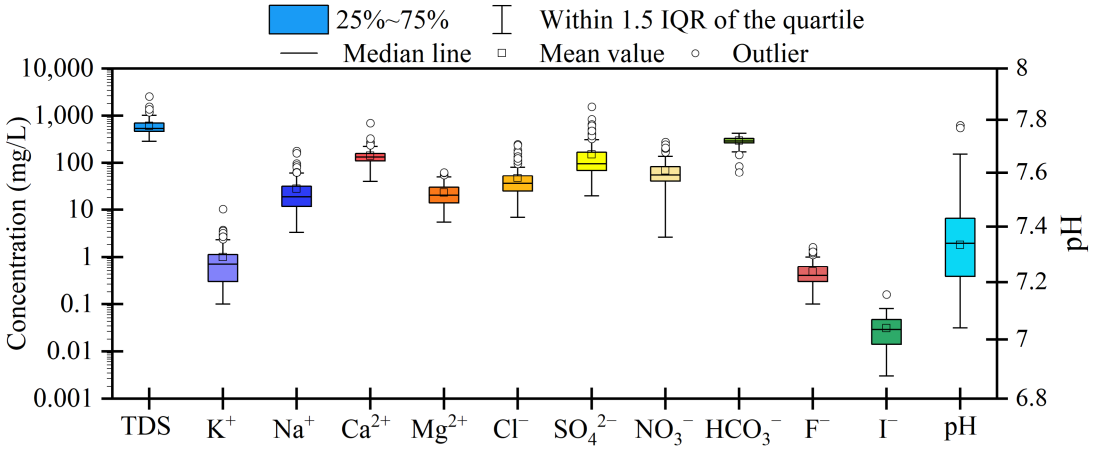



**Figure 2.** Box plots of hydrochemical parameters. The concentrations are plotted on a logarithmic scale (left axis, mg/L) and pH on the right axis. In each box, the square is the mean, the horizontal line is the median, the box spans the 25th–75th percentiles, the whiskers extend to 1.5 times the interquartile range, the circles are outliers and the colours are used only to distinguish the parameters.

TDS, $Ca^{2+}$, $Mg^{2+}$ and $HCO_3^-$ display a similar spatial pattern across the study area (Figure 3), following a broad trend of high values in the east and low values in the west. The high-value zones lie mainly in southern Yicheng District and the Tai'erzhuang area in the east, and they extend along the direction of groundwater flow, with the maxima clustered together. The low-value zones lie mostly in western Shanting District and the northern low mountains and hills of Xuecheng District, while the city centre lies between the two. These four ions therefore appear to share a common origin, controlled mainly by carbonate rock dissolution in the aquifer. $Cl^-$ and $SO_4^{2-}$ display a broadly similar pattern, increasing from the western low-value zone towards the east, with their high zones clustered in eastern Tai'erzhuang and southern Yicheng. Local point sources stand out ($SO_4^{2-}$ up to 1520.86 mg/L); such maxima may reflect human activity, but they may equally reflect the local dissolution of gypsum and halite, and the map alone cannot separate the two. The high zones of $Na^+$ occur mainly in Tai'erzhuang and southern Yicheng and coincide with the maxima of $Ca^{2+}$, $Cl^-$ and $SO_4^{2-}$. Because $Na^+$ rises together with the anions rather than replacing them, this coincidence does not by itself indicate cation exchange; it points to a common saline source, either evaporite dissolution or anthropogenic salt, and the exchange process is examined separately in Section 3.4.3. $K^+$ is fairly evenly distributed, with local highs in Yicheng District and northern Tai'erzhuang District, so its sources are more mixed and may involve both potash fertiliser and potassium-bearing minerals. The high zones of $NO_3^-$ lie mainly in western Shanting District, the north-central part of the city and northern Xuecheng District, which coincide with the areas of intensive farming in the west of the study area, so nitrate clearly reflects agricultural input. $F^-$ is highest in southern Tai'erzhuang District, but its concentration stays close to the detection limit over the whole area, so no separate mineral source can be resolved. $I^-$ is fairly evenly distributed and slightly higher in the west, but its overall level remains low (mean 0.031 mg/L). The pH

is also fairly uniform, with no clear maxima or minima, which points to a stable, weakly alkaline state and a strong buffering capacity.

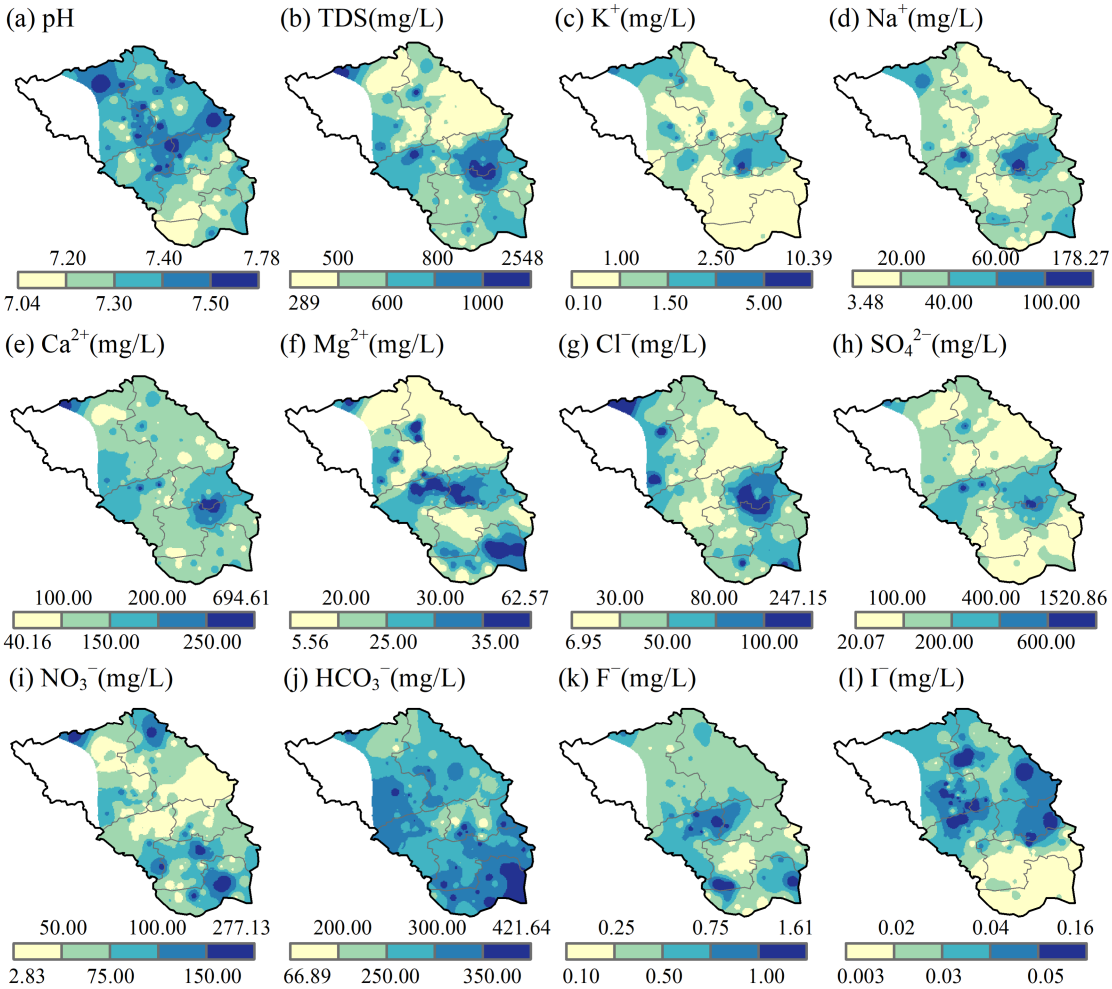



**Figure 3.** Spatial distribution of major hydrochemical parameters in the study area. All twelve panels share a single colour ramp, from the minimum (pale yellow) to the maximum (dark blue) of the mapped variable, so that the panels can be compared directly; the tick labels give the minimum, the intermediate class breaks and the maximum in mg/L, except for pH, which is dimensionless.

### *3.2. Hydrochemical Types*

The Piper and Durov diagrams provide a clear overview of the chemical composition and evolution of the groundwater [2]. The samples plot close together in both diagrams: most fall in the lower-left part of the cation triangle and the lower part of the anion triangle, which indicates that $Ca^{2+}$ and $HCO_3^-$ dominate the water chemistry (Figure 4). On average, $Ca^{2+}$ accounts for 69.93% of the cations in milliequivalents, and in 124 samples, it reaches 94.66%. Among the anions, $HCO_3^-$ accounts for 50.62% on average, with 80 samples at 61.07%, followed by $SO_4^{2-}$.

The water types were classified using the Shukarev classification. The dominant type is $HCO_3^-$Ca, which accounts for 58.78% of the samples. It is followed by the $HCO_3$·$SO_4$-Ca, $HCO_3^-$Ca·Mg and $SO_4$-Ca types, which together account for 40.46% and reflect the additional sulfate and nitrate contributed by human activity, whereas the $HCO_3^-$Na type accounts for only 0.76% of the samples. Together with the Piper diagram, this shows that the karst water is dominated by the $HCO_3^-$Ca type and, secondly, the $HCO_3$·$SO_4$-Ca type, which indicates a chemical evolution driven mainly by dissolution.

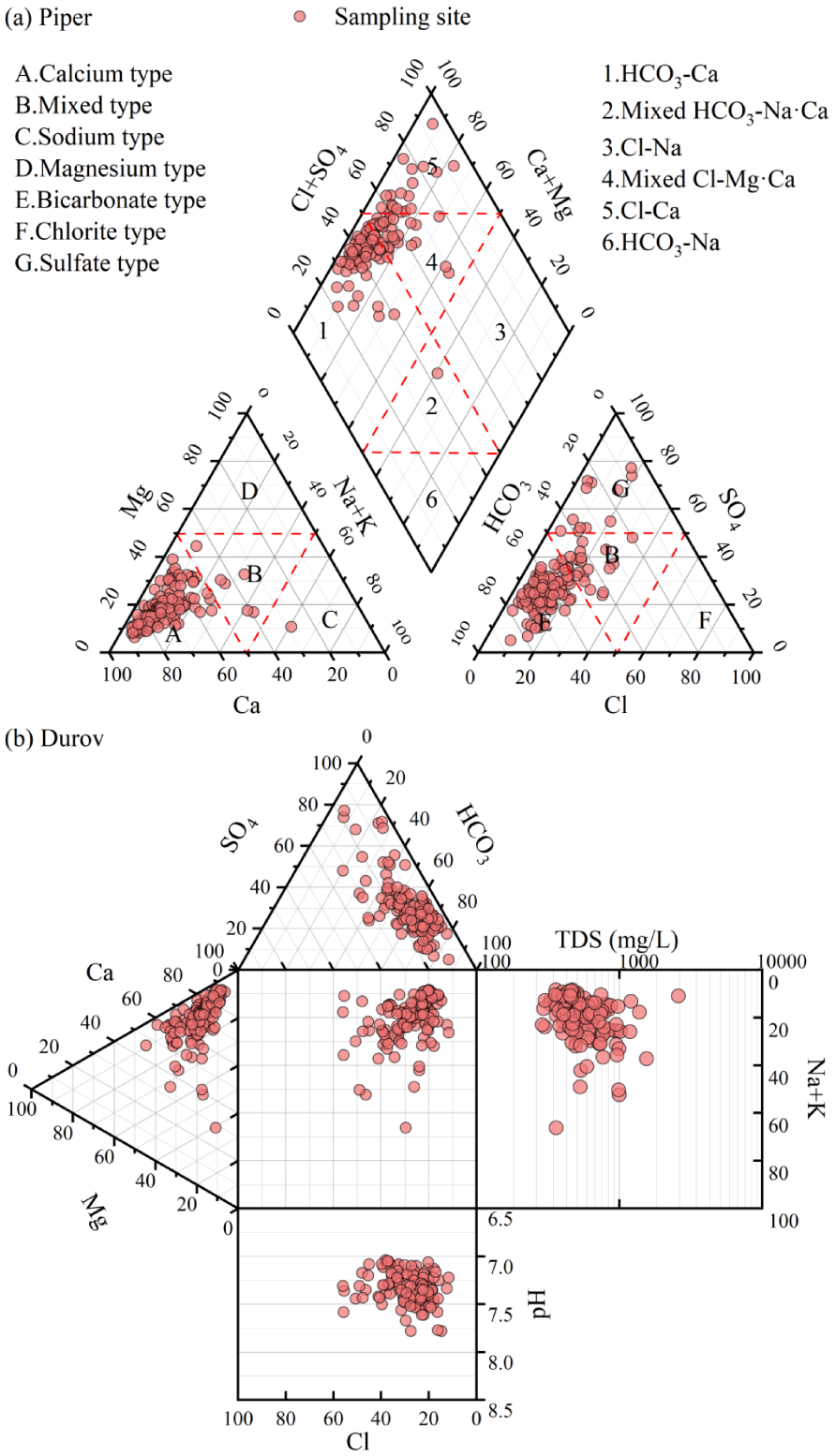



**Figure 4.** Piper (**a**) and Durov (**b**) diagrams of the major ions in the study area. In (**a**), the dashed lines delimit the cation sub-zones (A, calcium type; B, mixed type; C, sodium type; D, magnesium type; E, bicarbonate type; F, chloride type; G, sulfate type) and the anion sub-zones (1, $HCO_3$–Ca; 2, mixed $HCO_3$–Na–Ca; 3, Cl–Na; 4, mixed Cl–Mg–Ca; 5, Cl–Ca; 6, $HCO_3$–Na); the same symbols are used in both panels.

In space, the $HCO_3^-$Ca type occurs everywhere and dominates the west, centre and east of the study area, which shows that carbonate dissolution is the principal control on the water type. The $HCO_3$·$SO_4$-Ca type occurs in all zones and is related to local gypsum

dissolution and human activity. The $SO_4$-Na type appears only sporadically in the west, and the mixed-cation types occur mainly in the centre-east, where cation exchange and water–rock reaction along the flow path are stronger. Overall, the water type evolves from $HCO_3^-$Ca towards $HCO_3$·$SO_4$-Ca and $SO_4$-Ca along the flow direction, and aquifer lithology, water–rock reaction and human activity all play a part [38].

### *3.3. Ion Sources*

#### 3.3.1. Correlation Analysis

Correlation analysis indicates whether different ions in groundwater originate from a common source [6]. Here, TDS, total hardness, EC, $Ca^{2+}$ and $SO_4^{2-}$ are strongly correlated with one another, with coefficients above 0.85 ($p < 0.01$). The strongest pair is total hardness and $Ca^{2+}$ (0.96); TDS with $SO_4^{2-}$ and $Ca^{2+}$ gives 0.898 and 0.897, and $Ca^{2+}$ with $SO_4^{2-}$ gives 0.859. $Mg^{2+}$ also correlates fairly well with TDS and $SO_4^{2-}$ (Figure 5). These ions display similar spatial patterns and therefore probably share a common source [39].

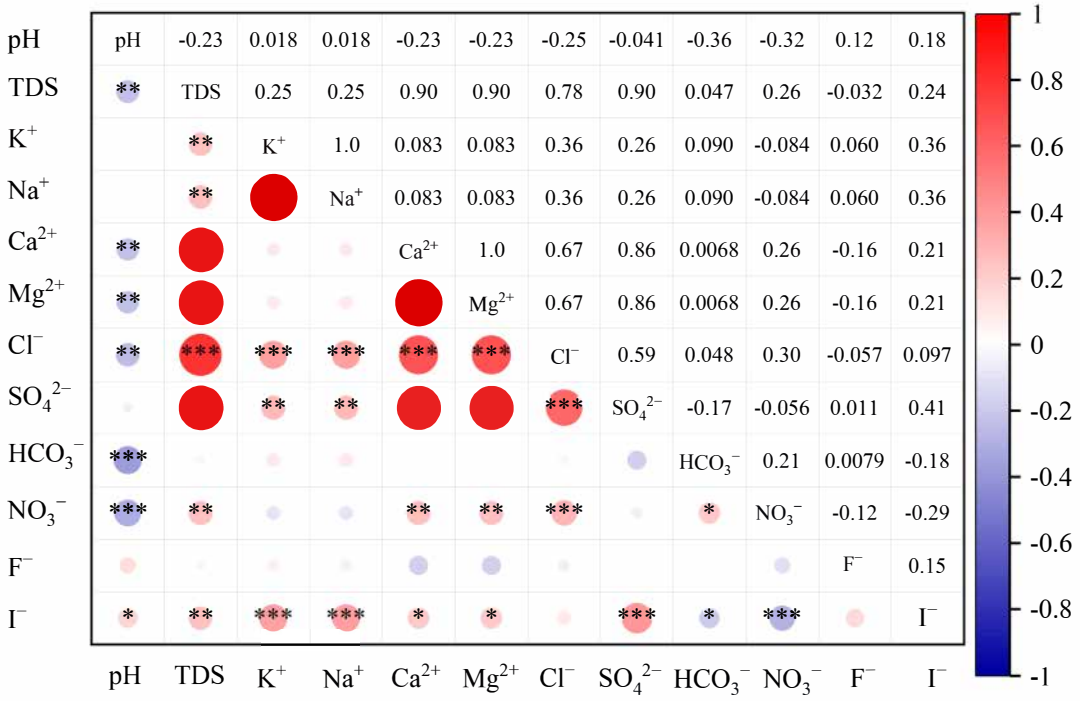



**Figure 5.** Pearson correlation matrix of the physicochemical parameters of groundwater. The colour and the size of each circle give the sign and the absolute value of the correlation coefficient, and the asterisks indicate the level of significance (* $p < 0.05$, ** $p < 0.01$, *** $p < 0.001$).

TDS and EC correlate clearly and positively with $Cl^-$, $Na^+$ and $K^+$, with coefficients between 0.581 and 0.791 ($p < 0.01$); EC with $Na^+$ and TDS with $Cl^-$ reach 0.719 and 0.780, $Na^+$ with $K^+$ and $Na^+$ with $Cl^-$ give 0.631 and 0.628, and $SO_4^{2-}$ with $Cl^-$ gives 0.586. $Cl^-$, $Na^+$ and $K^+$ therefore probably originate from evaporite dissolution or anthropogenic inputs. The pH correlates negatively with most ions, with coefficients of −0.364, −0.316 and −0.249 for $HCO_3^-$, $NO_3^-$ and $Cl^-$, respectively. $HCO_3^-$ shows little relationship with the other species (all absolute coefficients below 0.23), and $NO_3^-$ correlates weakly with all of them (at most 0.296). $F^-$, water temperature, DO and Eh likewise show no clear associations, so these species have sources distinct from those of the dominant ions. Because the $NO_3^-$ maxima occur in the farming zones of western Shanting District, the north-central part of the city and northern Xuecheng District, nitrate is derived mainly from fertiliser use, with further contributions from manure, sewage and sewage sludge spread on farmland as fertiliser.

### 3.3.2. Dissolution Processes

Ion ratios can reveal the sources of the chemical components in groundwater. In general, $Na^+$, $K^+$ and $Cl^-$ are derived from the dissolution of evaporite and silicate rocks, cation exchange and anthropogenic inputs [4,6]. Below, r(X) denotes the milliequivalent concentration of ion X.

The ratio $r(Na^+ + K^+)/r(Cl^-)$ indicates the main source of $Na^+$ and $K^+$. A value of 1 indicates that evaporite dissolution dominates, a value above 1 that silicate dissolution and cation exchange contribute, and a value below 1 that anthropogenic inputs are likely, since they raise $Cl^-$ [6]. In the plot of this ratio (Figure 6a), 71% of the points fall below the 1:1 line, with a mean of 0.95 and a median of 0.78. $Na^+$ and $K^+$ are therefore deficient relative to $Cl^-$, and $Cl^-$ may be enriched by human influence, through sewage, manure, industrial salt or the dissolution of halite in the evaporite beds. The remaining 29% of the points lie above the 1:1 line, so that part of the water is affected by silicate dissolution and cation exchange.

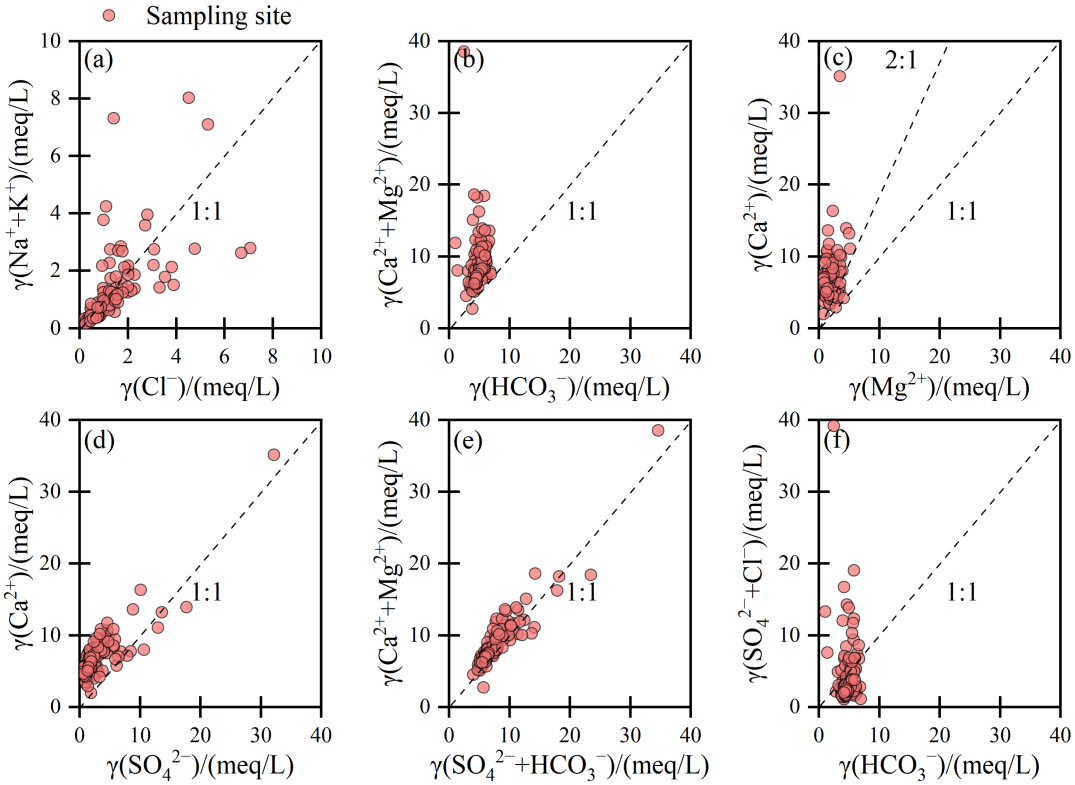



**Figure 6.** Ion ratio relationships of karst groundwater: (**a**) γ ($Na^+ + K^+$) vs. γ ($Cl^-$); (**b**) γ ($Ca^{2+} + Mg^{2+}$) vs. γ ($HCO_3^-$); (**c**) γ ($Ca^{2+}$) vs. γ ($Mg^{2+}$); (**d**) γ ($Ca^{2+}$) vs. γ ($SO_4^{2-}$); (**e**) γ ($Ca^{2+} + Mg^{2+}$) vs. γ ($SO_4^{2-} + HCO_3^-$); (**f**) γ ($SO_4^{2-} + Cl^-$) vs. γ ($HCO_3^-$). γ (X) is the milliequivalent concentration of ion X, the quantity written r(X) in the text; the dashed lines are the 1:1 reference lines, and the additional dashed line in (**c**) is the 2:1 line.

The ratio $r(Ca^{2+} + Mg^{2+})/r(HCO_3^-)$ indicates the sources of $Ca^{2+}$ and $Mg^{2+}$. A value close to 1 means that these two ions are derived mainly from carbonate dissolution [4]. In Figure 6b, 99% of the points lie above the 1:1 line, and the sum of $Ca^{2+}$ and $Mg^{2+}$ clearly exceeds $HCO_3^-$, so $Ca^{2+}$ and $Mg^{2+}$ have sources in addition to carbonate dissolution. Sulfate minerals such as gypsum in the area supply further $Ca^{2+}$, which is consistent with the strong positive correlation between $Ca^{2+}$ and $Mg^{2+}$ noted above. This ratio only gives reliable results when no other sources of $Ca^{2+}$ and $Mg^{2+}$ are present, and it is therefore

interpreted here together with the sulfate and source-apportionment results rather than on its own.

The ratio $r(Ca^{2+})/r(Mg^{2+})$ indicates whether the carbonate minerals are derived mainly from dolomite or calcite weathering: a value near 1 indicates dolomite dissolution, a value above 2 calcite dissolution and a value between 1 and 2 the dissolution of both [4]. In Figure 6c, 88% of the points lie above the 2:1 line, with a mean of 4.50 and a median of 3.97, so $Ca^{2+}$ and $Mg^{2+}$ are derived mainly from calcite dissolution, with only a small contribution from dolomite. About 12% of the points fall between 1 and 2, which indicates either local mixing of calcite and dolomite dissolution or, more simply, the dissolution of compositionally intermediate carbonates such as the dolomitic limestone and calcic dolomite of the Cambrian and Ordovician sequences.

The ratio $r(Ca^{2+})/r(SO_4{}^{2-})$ indicates whether $Ca^{2+}$ is affected by evaporite dissolution [40]. In Figure 6d, 95% of the points lie above the 1:1 line, with a mean of 3.23 and a median of 3.13. $Ca^{2+}$ and $SO_4{}^{2-}$ do not co-vary along the 1:1 line, so $Ca^{2+}$ is only slightly affected by evaporite dissolution and is derived mainly from carbonate dissolution. $SO_4{}^{2-}$, by contrast, may have sources other than evaporite minerals, such as sulfide oxidation and anthropogenic inputs; the sulfate concentrations are too high to be explained by sulfide oxidation alone unless a sulfide-rich source, such as the coal measures of the Zaozhuang basin, is available. Only about 5% of the points lie below the 1:1 line, which suggests a gypsum signal in a few local samples [40]. Pyrite is a common accessory mineral in the coal measures and also occurs disseminated in the carbonate rocks, so part of the sulfate may be produced within the aquifer itself.

The ratio $r(Ca^{2+} + Mg^{2+})/r(HCO_3{}^- + SO_4{}^{2-})$ indicates whether evaporite and carbonate minerals jointly control the water chemistry [6]. In Figure 6e, 90% of the points lie above the 1:1 line, so anions such as $NO_3{}^-$ and $Cl^-$ also contribute to the charge balance in addition to carbonate and evaporite dissolution. This is consistent with the relatively high $NO_3{}^-$ concentrations in the area and shows that nitrate and other anthropogenic inputs influence the water chemistry.

The ratio $r(Cl^- + SO_4{}^{2-})/r(HCO_3{}^-)$ indicates the relative contributions of carbonate, silicate and evaporite rocks to the water chemistry [6]. In Figure 6f, 75% of the points lie below the 1:1 line, and the mean ratio is 0.70, so $HCO_3{}^-$ dominates and carbonate dissolution governs the chemistry, with only a minor contribution from evaporite minerals. About 25% of the points lie above the 1:1 line, where $Cl^- + SO_4{}^{2-}$ is enriched relative to $HCO_3{}^-$; these samples are more strongly affected by evaporite dissolution or anthropogenic inputs. These ratios describe the balance between carbonate and evaporite weathering, but they do not identify the source of the sulfate itself, which may be gypsum dissolution, the oxidation of disseminated pyrite or sulfate fertilisers.

### *3.4. Analysis of Controlling Factors*

#### 3.4.1. Identification of Controlling Factors

As groundwater reacts with the surrounding rock, its chemical composition changes, and the study of this reaction reveals the mechanism of chemical evolution. The Gibbs diagram provides a qualitative indication of whether precipitation, rock weathering or evaporation governs the water chemistry [11]. Most of the samples fall in the rock-weathering zone (Figure 7), so rock weathering and dissolution are the dominant controls. At the same time, some high-TDS samples drift towards the evaporation zone, and TDS correlates clearly with the $Cl^-/(Cl^- + HCO_3{}^-)$ ratio ($r = 0.728$). This association alone does not demonstrate evaporation in a sub-humid, monsoon-influenced setting, however, and a longer residence time and mixing are equally plausible explanations. No samples plot near the precipitation zone, so precipitation has little influence on the solute content. For nearly

all samples, $\rho(Na^+)/\rho(Na^+ + Ca^{2+})$ and $\rho(Cl^-)/\rho(Cl^- + HCO_3^-)$ are below 0.5 (96.9% and 98.5% of the samples, with means of 0.15 and 0.13), so $Ca^{2+}$ outweighs $Na^+$ and $HCO_3^-$ outweighs $Cl^-$ in this karst water. A few samples (about 3.1% and 1.5%) have values above 0.5 for these ratios and may be affected by human activity [41,42]. Here, ρ(X) denotes the mass concentration of component X.

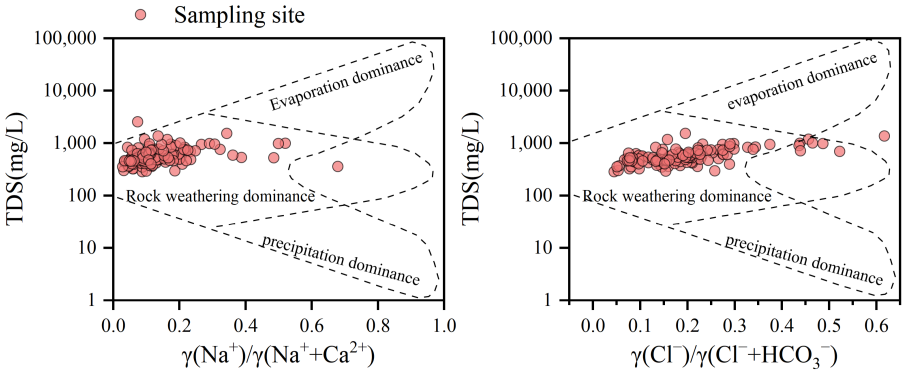



**Figure 7.** Gibbs diagram of karst groundwater in the study area. The left panel plots TDS against γ $(Na^+)/(\gamma\ (Na^+) + \gamma\ (Ca^{2+}))$ and the right panel plots TDS against γ $(Cl^-)/(\gamma\ (Cl^-) + \gamma\ (HCO_3^-))$; the dashed outlines delimit the precipitation-dominance, rock-weathering-dominance and evaporation-dominance fields.

The water chemistry is also constrained by the dissolution of evaporite, carbonate and silicate rocks. End-member diagrams based on $N(Mg^{2+})/N(Na^+)$, $N(Ca^{2+})/N(Na^+)$ and $N(HCO_3^-)/N(Na^+)$ can identify the rock weathering that supplies the solutes [43], where N(X) denotes the milliequivalent concentration of component X. In Figure 8a, the points lie between the silicate and carbonate end-members and clearly away from the evaporite end-member. The means and medians of $N(Ca^{2+})/N(Na^+)$ are 4.78 and 4.15, and those of $N(HCO_3^-)/N(Na^+)$ are 7.00 and 6.09, both far above the silicate weathering end-member ($Ca/Na \approx 0.35$, $HCO_3/Na \approx 2$). Carbonate weathering and dissolution therefore dominate the water chemistry, with a few samples affected by silicate weathering. In Figure 8b, the points lie away from the carbonate end-member; the means and medians of $N(Mg^{2+})/N(Na^+)$ are 1.18 and 0.96, with a clear linear trend, which may reflect cation exchange and the dissolution of magnesium-bearing minerals such as dolomite [43]. Dissolved silica is present in every sample ($H_2SiO_3$ 9.8–46.0 mg/L, mean 15.9 mg/L; Section 2.2), which shows that silicate minerals do weather in the aquifer, but the amounts involved are small: the Ca/Na and HCO3/Na ratios lie far above the silicate end-member, and no sample approaches it.

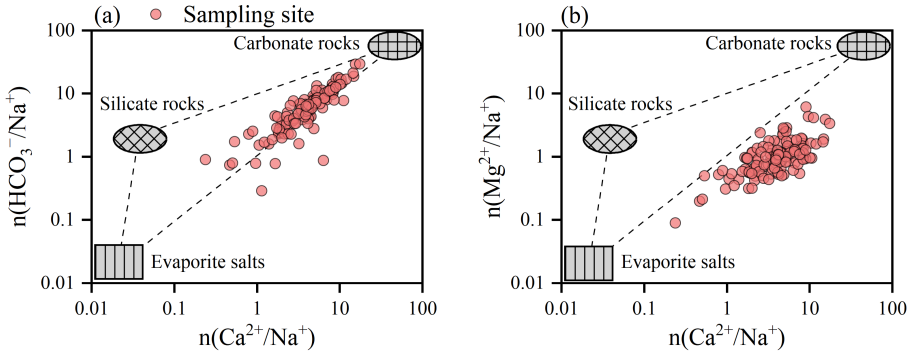



**Figure 8.** Ion end-member diagram of karst groundwater in the study area: (**a**) $n(HCO_3^-)/n(Na^+)$ vs. $n(Ca^{2+})/n(Na^+)$; (**b**) $n(Mg^{2+})/n(Na^+)$ vs. $n(Ca^{2+})/n(Na^+)$. n(X) is the milliequivalent concentration of component X, and the dashed lines delimit the carbonate, silicate and evaporite end-member fields.

### 3.4.2. Mineral Dissolution Equilibrium

The saturation indices of calcite and dolomite in this karst water are strongly correlated (r = 0.781, $p < 0.01$; Figure 9b). As shown in Figure 9a, the SI of calcite ranges from −0.10 to 0.77 (mean 0.41), and 98.5% of the samples have values above 0, while the SI of aragonite ranges from −0.24 to 0.63 (mean 0.26), and 93.9% of the samples are above 0, so calcite and aragonite are mostly in equilibrium or slightly oversaturated. The SI of dolomite ranges from −1.19 to 0.68 (mean −0.20), and only 26.7% of the samples are above 0, so dolomite is generally undersaturated and continues to dissolve. This contrast between calcite and dolomite points to cation exchange in the water. The SI of gypsum ranges from −2.11 to 0.24 (mean −1.27), and 99.2% of the samples are below 0, so gypsum is clearly undersaturated and retains a strong tendency to dissolve [36].

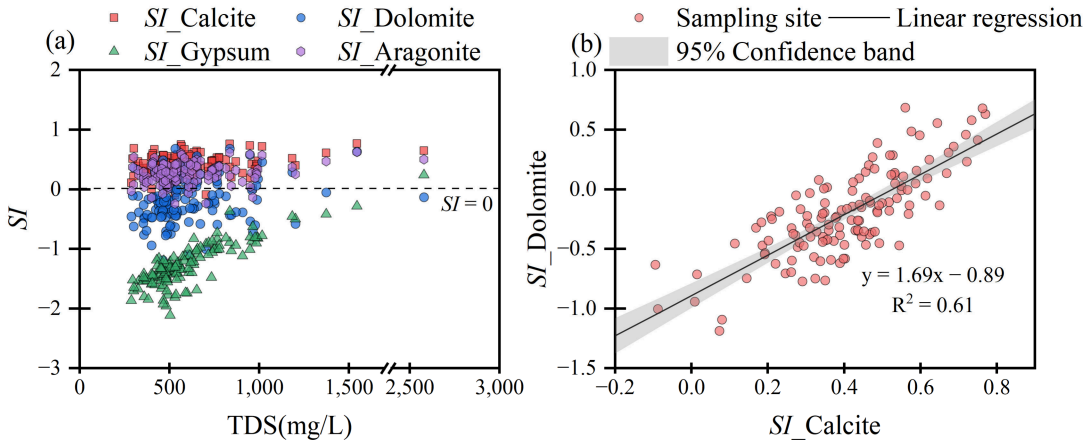



**Figure 9.** Saturation indices of different minerals for karst groundwater in the study area: (**a**) saturation indices of calcite, dolomite, gypsum and aragonite plotted against TDS, with the dashed line marking SI = 0; (**b**) saturation index of dolomite against that of calcite, with the solid line giving the linear regression and the grey band its 95% confidence interval. The indices were computed with PHREEQC 3 using the phreeqc.dat database, the Debye-Hückel activity model and the measured in situ temperature of each sample.

Taken together, the karst water is close to saturation with respect to the carbonate minerals but clearly undersaturated with respect to the sulfate minerals: carbonate dissolution has nearly reached equilibrium, whereas sulfate minerals such as gypsum continue to dissolve. The water therefore still has a considerable capacity to dissolve the aquifer medium [44].

### 3.4.3. Cation Exchange

Cation exchange (adsorption) is the process by which aquifer particles take up some cations and release part of those already held, thereby modifying the chemistry of natural water. It is widespread in aquifers and strongly influences the evolution of groundwater [45]. It is usually identified from the milliequivalent ratio of $N[(Na^+ + K^+) - Cl^-]$ to $N[(Ca^{2+} + Mg^{2+}) - (SO_4^{2-} + HCO_3^-)]$: when cation exchange is active, this ratio approaches −1. In the plot of these two terms (Figure 10a), most points show a clear negative trend, with a correlation of −0.855 ($p < 0.01$) and a fitted slope of −1.115, close to −1, so cation exchange is widespread in this karst water.

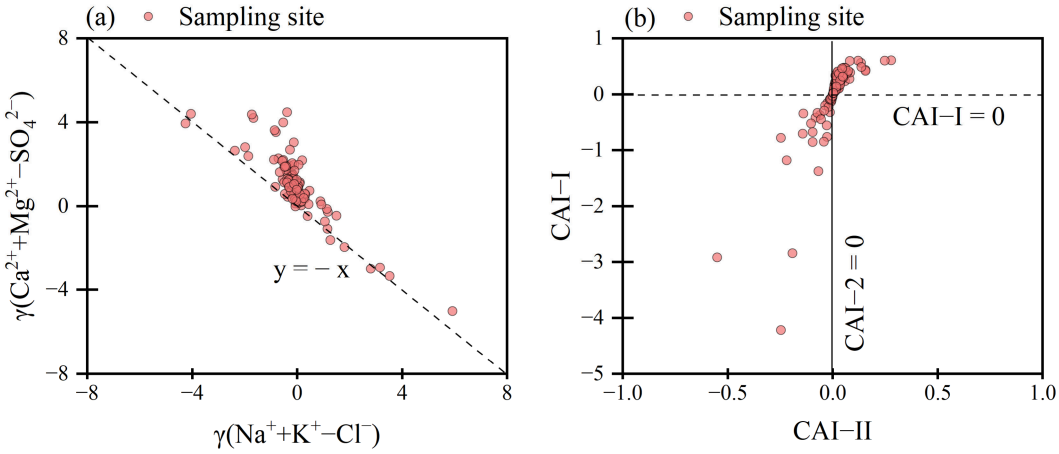



**Figure 10.** Cation exchange and chloro-alkaline indices of karst groundwater in the study area: (**a**) γ ($Ca^{2+}$ + $Mg^{2+}$ − $SO_4^{2-}$) vs. γ ($Na^+$ + $K^+$ − $Cl^-$), where the dashed line is y = −x, the trend expected when cation exchange controls the chemistry; (**b**) CAI−1 vs. CAI−2, where the dashed line marks CAI−1 = 0 and the solid line marks CAI−2 = 0.

The chloro-alkaline indices ($CAI^-1$ and $CAI^-2$) indicate the type and intensity of cation exchange. Positive values indicate that $Na^+$ and $K^+$ in the water replace $Ca^{2+}$ and $Mg^{2+}$ in the aquifer, negative values the reverse, and larger absolute values indicate stronger exchange [45]. In Figure 10b, 71.0% of the samples have both $CAI^-1$ and $CAI^-2$ positive, so in most of the karst water, $Na^+$ and $K^+$ are taken up by the aquifer materials, while $Ca^{2+}$ and $Mg^{2+}$ are released into the water, which is consistent with the deficiency of $Na^+$ relative to $Cl^-$ noted above. About 29% of the samples have negative values, so, locally, $Ca^{2+}$ and $Mg^{2+}$ replace $Na^+$ in the aquifer. The mean absolute value of $CAI^-1$ reaches 0.369, so cation exchange is relatively strong overall. Together with the clear positive correlation between $Na^+$ and $SO_4^{2-}$ ($r = 0.510$, $p < 0.01$), this suggests that $Na^+$ is derived not only from evaporite dissolution but also from water-rock reaction in which sulfuric acid participates in carbonate dissolution. Cation exchange therefore modifies the ionic balance of this karst water, but it cannot be the main control on its composition: it transfers cations between the water and the solid phase without adding solute mass, the exchangeable $Na^+$ involved is small compared with the $Na^+$ carried by the salt factor, and its effect is probably concentrated in the clay-rich interbeds and residual clay filling the karst fissures, where the exchange capacity is highest.

### 3.4.4. Influence of Human Activities

Human activity influences the chemical evolution of groundwater and surface water and is reflected mainly in the concentrations of $SO_4^{2-}$, $Cl^-$, $NO_3^-$ and $Na^+$. $SO_4^{2-}$ is derived largely from the dissolution of sulfate minerals such as gypsum and anhydrite and the oxidation of sulfide minerals in the coal measures of the Zaozhuang basin [36]; the coal measures lie below the karst aquifer, so this sulfate can reach the wells only along faults, abandoned shafts and mine workings, or where mine water is discharged at the surface, and sulfate applied to farmland as ammonium sulfate, single superphosphate or gypsum must also be considered, whereas $Cl^-$, $NO_3^-$ and $Na^+$ are associated with farming, domestic sewage and industrial salt [46,47]. The plot of $N(SO_4^{2-})/N(Ca^{2+})$ against $N(NO_3^-)/N(Ca^{2+})$ can distinguish the roles of different human activities, since farming tends to raise $N(NO_3^-)/N(Ca^{2+})$ and mining to raise $N(SO_4^{2-})/N(Ca^{2+})$. In Figure 11a, most points show higher $N(NO_3^-)/N(Ca^{2+})$, so farming is the leading human influence, which is consistent with the $NO_3^-$ exceedance rate of 68.7% in the area. Some

points also show higher $N(SO_4^{2-})/N(Ca^{2+})$, and the $SO_4^{2-}$ exceedance rate is 12.98%, so industry and mining also affect the water to some degree [46–48].

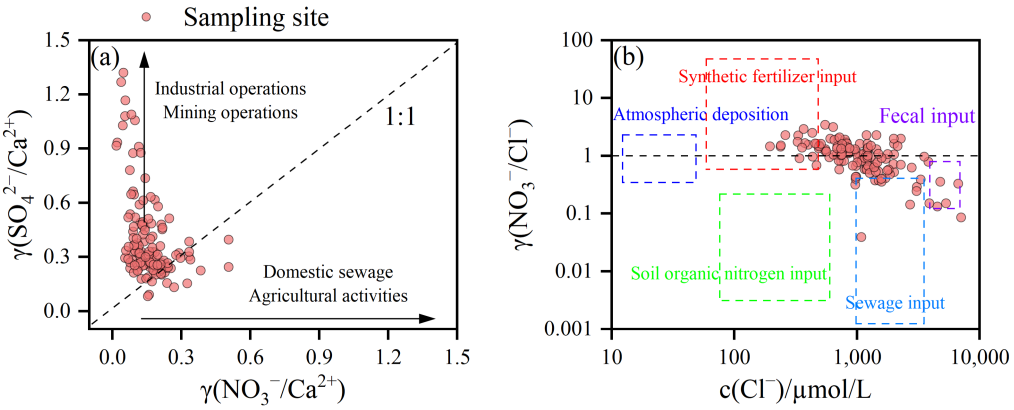



**Figure 11.** Influence of human activities on karst groundwater in the study area: (**a**) γ $(SO_4^{2-})$/γ $(Ca^{2+})$ vs. γ $(NO_3^-)$/γ $(Ca^{2+})$, where the dashed line is the 1:1 line and the arrows indicate the trends produced by industrial and mining operations and by domestic sewage and agricultural activities; (**b**) γ $(NO_3^-)$/γ $(Cl^-)$ vs. the molar concentration of $Cl^-$, where the dashed boxes mark the ranges typical of atmospheric deposition, synthetic fertiliser, soil organic nitrogen, faecal and sewage inputs and the horizontal dashed line marks a ratio of 1.

$NO_3^-$ and $Cl^-$ are useful markers of human activity, and the ratios $N(NO_3^-)/N(Na^+)$ and $N(Cl^-)/N(Na^+)$ are therefore commonly used to identify the influence of human activity on nitrate in groundwater [46]. In Figure 11b, the samples generally show high $N(NO_3^-)/N(Na^+)$ and $N(Cl^-)/N(Na^+)$ and drift towards the farming field, so the karst water is also influenced by farming. The accumulation of nitrate is closely related to fertiliser, domestic sewage and aquaculture wastewater, whereas $Cl^-$, a conservative tracer, remains fairly low. The water is therefore only slightly affected by mining brine or seawater intrusion, and the anthropogenic influence is dominated by non-point agricultural inputs.

### *3.5. Quantitative Assessment of Sources of Karst Water Chemical Components*

#### 3.5.1. Identification of Influencing Factors

Applied to the ten measured ions, PMF resolves four factors. The four-factor solution reaches Q = 874.2 against an expected value of $Q_{exp}$ = 746, so $Q/Q_{exp}$ = 1.17; the standardised residuals have a root-mean-square of 1.83 and only 3.9% of them exceed four times the uncertainty (Table 2). The solution was selected on the basis of $Q/Q_{exp}$ and the hydrogeochemical interpretability of the factors, whereas with eight factors, $Q/Q_{exp}$ falls to 0.54, which indicates over-fitting. The four factors were reproduced in 89–100% of the 200 bootstrap runs, which indicates a stable solution.

Factor F1 accounts for 36.85% of the total solute mass (bootstrap 5th–95th percentile of 32.41–47.08%). Its profile is dominated by $HCO_3^-$ (459.84 mg/L) and $Ca^{2+}$ (86.94 mg/L), with subordinate $Mg^{2+}$ (28.06 mg/L) and $Na^+$ (17.52 mg/L). It contributes 72.75% of the $HCO_3^-$, 56.48% of the $Mg^{2+}$, 28.45% of the $Ca^{2+}$, 80.04% of the $F^-$ and 45.97% of the $K^+$ in the samples. This is the signature of carbonate rock weathering: the dissolution of calcite and dolomite by soil $CO_2$ and carbonic acid releases $Ca^{2+}$, $Mg^{2+}$ and $HCO_3^-$, and the saturation indices show that calcite and dolomite approach equilibrium while gypsum stays undersaturated. F1 is therefore called the carbonate weathering factor. The Ordovician and Cambrian limestones and dolomites hold the karst fissures that supply the wells of the area, and this factor accounts for the largest share of the solute mass (36.85%).

Factor F2 accounts for 27.41% of the total solute mass (bootstrap 15.30–35.74%). It is the only factor with a strong $NO_3^-$ signal (145.01 mg/L) and it alone supplies 95.62%

of the $NO_3^-$ of the samples, together with 144.86 mg/L of $HCO_3^-$, 110.74 mg/L of $Ca^{2+}$ and 46.24 mg/L of $Cl^-$. Nitrate entering the aquifer with the carbonate it dissolves gives exactly this combination: fertiliser and manure nitrogen is oxidised to nitric acid in the soil zone, and that acid then weathers the carbonate rock and releases $Ca^{2+}$ and $HCO_3^-$ together with the $NO_3^-$. The factor matches the spatial pattern of the water chemistry, where $NO_3^-$ is high in the farming districts of the city and the northern part of Xuecheng. F2 is therefore called the agricultural nitrogen factor. The nitrogen carried by this factor is therefore attributed to agricultural and anthropogenic sources as a group.

**Table 2.** PMF factor profiles of karst groundwater in the study area.

| Parameter | F1 | F2 | F3 | F4 |
|---|---|---|---|---|
| $K^+$ | 0.985 (46.0) | 0.000 (0.0) | 0.000 (0.0) | 3.852 (54.0) |
| $Na^+$ | 17.522 (28.7) | 0.000 (0.0) | 0.000 (0.0) | 145.030 (71.3) |
| $Ca^{2+}$ | 86.944 (28.4) | 110.736 (35.8) | 87.896 (35.8) | 0.000 (0.0) |
| $Mg^{2+}$ | 28.062 (56.5) | 5.779 (11.5) | 5.586 (14.0) | 29.834 (18.0) |
| $Cl^-$ | 0.000 (0.0) | 46.236 (43.9) | 10.239 (12.2) | 152.052 (43.9) |
| $SO_4^{2-}$ | 0.619 (0.2) | 0.000 (0.0) | 220.162 (83.9) | 172.518 (15.9) |
| $NO_3^-$ | 6.562 (4.4) | 145.014 (95.6) | 0.000 (0.0) | 0.000 (0.0) |
| $HCO_3^-$ | 459.836 (72.7) | 144.864 (22.6) | 1.784 (0.4) | 89.602 (4.3) |
| $F^-$ | 0.807 (80.0) | 0.080 (7.8) | 0.022 (2.8) | 0.314 (9.4) |
| $I^-$ | 0.041 (64.3) | 0.000 (0.0) | 0.015 (29.9) | 0.012 (5.8) |
| Contribution (%) | 36.85 | 27.41 | 24.81 | 10.92 |
| Bootstrap 5th–95th percentile (%) | 32.41–47.08 | 15.30–35.74 | 18.71–28.07 | 7.49–16.46 |
| Bootstrap mapping ratio | 1.00 | 1.00 | 1.00 | 0.89 |

Note: S/N is the signal-to-noise ratio of the species and 'Weak' marks the two species whose uncertainty was multiplied by three. The first value in each cell is the concentration of the species in the factor profile (mg/L) and the value in brackets is the share of that species that the factor carries (%). F1: carbonate weathering; F2: agricultural nitrogen input; F3: sulfate mineral dissolution; F4: halite dissolution with anthropogenic salt input.

Factor F3 accounts for 24.81% of the total solute mass (bootstrap 18.71–28.07%). Its profile is led by $SO_4^{2-}$ at 220.16 mg/L, followed by $Ca^{2+}$ at 87.90 mg/L, with only minor $Cl^-$ and $Mg^{2+}$. It contributes 83.92% of the $SO_4^{2-}$ and 35.75% of the $Ca^{2+}$ in the samples. The combination is that of gypsum and anhydrite dissolution, which releases $SO_4^{2-}$ and $Ca^{2+}$ in equal equivalents; the saturation indices show gypsum to be clearly undersaturated over the whole area, so these minerals are still dissolving. Part of the sulfate may also come from the oxidation of sulfide minerals in the coal-bearing Carboniferous–Permian beds inside the Zaozhuang basin, which adds sulfate as sulfuric acid; the acid is then neutralised by dissolving carbonate, so the accompanying cation is $Ca^{2+}$ supplied by the carbonate rather than the sulfide, and the factor is named for the sulfate minerals rather than for a single mineral. Sulfate is the second most abundant anion in the area (mean 151.39 mg/L), and this factor is its largest single contributor, in line with the high-$SO_4^{2-}$ zones that surround the mining districts.

Factor F4 accounts for 10.92% of the total solute mass (bootstrap 7.49–16.46%), the smallest of the four. Its profile is characterised by $Na^+$ (145.03 mg/L), $Cl^-$ (152.05 mg/L), $SO_4^{2-}$ (172.52 mg/L) and $K^+$ (3.85 mg/L). It contributes 71.32% of the $Na^+$, 43.89% of the $Cl^-$, 54.03% of the $K^+$ and 15.89% of the $SO_4^{2-}$ in the samples. A Na-Cl-K-rich end member with subordinate sulfate points to halite and other evaporite salts, together with the salts that human activity brings into the aquifer, in particular the NaCl of household sewage, animal waste and industrial salt. The two cannot be separated with the species available here because halite dissolution and anthropogenic salt input carry the same $Na^+/Cl^-$ signature, so F4 is called the halite–anthropogenic salt factor and its share is reported as

mixed rather than purely natural or purely anthropogenic. $Cl^-$ stays low over most of the area (mean 47.22 mg/L), and the factor is concentrated in the eastern and urban districts, where the pressure from sewage and industry is greatest.

Summing up, the four factors account for 36.85%, 27.41%, 24.81% and 10.92% of the solute mass. The share of each ion is given in Table 3. $HCO_3^-$ and $Mg^{2+}$ come mainly from carbonate weathering (72.75% and 56.48%), $NO_3^-$ almost entirely from agricultural nitrogen (95.62%), $SO_4^{2-}$ from sulfate mineral dissolution (83.92%), and $Na^+$, $Cl^-$ and $K^+$ from the halite–anthropogenic salt factor (71.32%, 43.89% and 54.03%). $Ca^{2+}$ and $Cl^-$ are shared between factors, as expected for ions that take part in more than one process. The two natural processes, carbonate weathering and sulfate mineral dissolution, carry 61.67% of the solute mass, and the two human-influenced factors, agricultural nitrogen and halite–anthropogenic salt, carry 38.33%. Because F3 and F4 each combine a natural process with an anthropogenic process, these two figures represent an upper bound for the natural share and a lower bound for the human share.

**Table 3.** Contribution rates of different solute sources to karst groundwater in the study area (%).

| Source | $K^+$ | $Na^+$ | $Ca^{2+}$ | $Mg^{2+}$ | $Cl^-$ | $SO_4^{2-}$ | $NO_3^-$ | $HCO_3^-$ | $F^-$ | $I^-$ |
|---|---|---|---|---|---|---|---|---|---|---|
| Carbonate weathering | 45.97 | 28.68 | 28.45 | 56.48 | 0.00 | 0.19 | 4.38 | 72.75 | 80.04 | 64.30 |
| Agricultural nitrogen input | 0.00 | 0.00 | 35.80 | 11.49 | 43.88 | 0.00 | 95.62 | 22.64 | 7.83 | 0.00 |
| Sulfate mineral dissolution | 0.00 | 0.00 | 35.75 | 13.98 | 12.23 | 83.92 | 0.00 | 0.35 | 2.76 | 29.88 |
| Halite–anthropogenic salt | 54.03 | 71.32 | 0.00 | 18.04 | 43.89 | 15.89 | 0.00 | 4.26 | 9.36 | 5.82 |

Note: The contribution rates are the shares of each ion's modelled mass that are assigned to each PMF factor (%). The four factors sum to 100% for every ion.

Two processes that appear in the Introduction do not form factors of their own. Silicate weathering releases $Na^+$, $K^+$ and dissolved silica; dissolved silica is present in every sample (mean 15.9 mg/L), but the Ca/Na and HCO3/Na ratios of the water lie far above the silicate end-member (Section 3.4.1), so silicate weathering supplies only a small part of the solute mass, and a sensitivity run in which $H_2SiO_3$ was added as an eleventh variable returned the same four factors. Cation exchange is not a source at all: it exchanges one cation for another without adding solute mass, so it appears in the apportionment as a redistribution of $Na^+$, $K^+$, $Ca^{2+}$ and $Mg^{2+}$ among the factors rather than as a factor of its own. Its direction and relative intensity are reported in Section 3.4.3 ($CAI^-1$ and $CAI^-2$ positive in 71.0% of the samples, mean $|CAI^-1| = 0.369$), and the exchangeable $Na^+$ involved is small compared with the $Na^+$ carried by the halite–anthropogenic salt factor.

### 3.5.2. Source Contribution Apportionment of Karst Water

Section 3.5.1 identified the four factors and their chemical profiles; this section quantifies how much of each ion, and of the total solute mass, each factor supplies in each sample and examines what those shares imply for the origin of the water chemistry. The contributions were computed for every sample and every ion (Table 3). The measured and modelled concentrations agree well over most of the range (Figure 12). The coefficient of determination is 0.999 for$SO_4^{2-}$ and $HCO_3^-$, 0.949 for $Ca^{2+}$, 0.927 for $NO_3^-$, 0.896 for $Na^+$ and 0.852 for $Cl^-$, with a mean of 0.801 for the eight major ions. The two species that were down-weighted as 'Weak', $F^-$ and $I^-$, are reproduced poorly ($R^2$ values of −0.05 and 0.16): their concentrations lie close to the detection limit, where the analytical uncertainty is of the same order as the spatial variability, so no separate source is assigned to them. Sensitivity runs in which all species were treated as Strong, $H_2SiO_3$ was added as an eleventh variable and the error fraction and extra modelling uncertainty were varied gave the same four factors and the same shares.

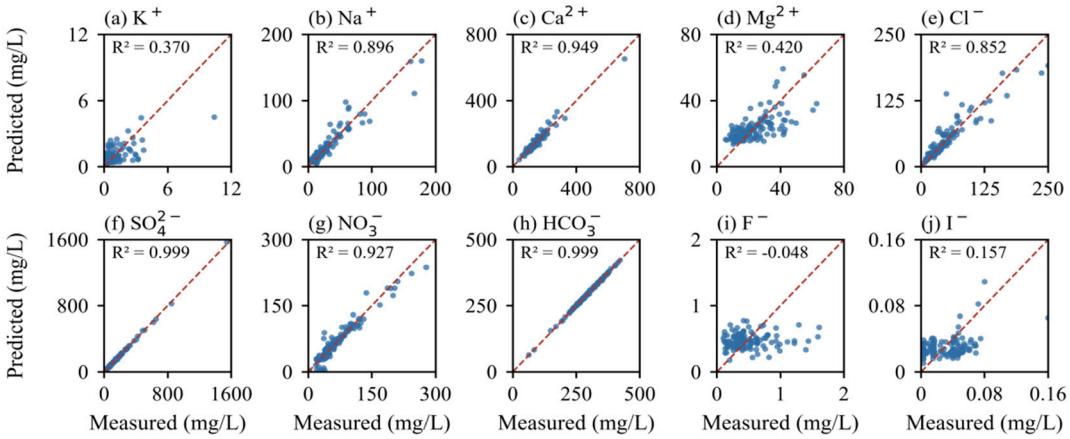



**Figure 12.** Relationship between the predicted and measured concentrations of karst groundwater in the study area: (**a**) $K^+$; (**b**) $Na^+$; (**c**) $Ca^{2+}$; (**d**) $Mg^{2+}$; (**e**) $Cl^-$; (**f**) $SO_4{}^{2-}$; (**g**) $NO_3{}^-$; (**h**) $HCO_3{}^-$; (**i**) $F^-$; (**j**) $I^-$. The blue circles are the individual samples, the red dashed line is the 1:1 line and $R^2$ is the coefficient of determination.

Table 3 gives the share of each ion that is assigned to each of the four PMF factors. The weathering and dissolution of carbonate and sulfate minerals are thus the chief control on the chemical composition of this karst water. This is supported by the strong $Ca^{2+}$-$SO_4{}^{2-}$ correlation (r = 0.859) and the saturation indices, which show that calcite is close to equilibrium while gypsum remains clearly undersaturated [49]. No separate silicate factor appears in Table 3: silicate weathering supplies only a small part of the solute mass, as the end-member ratios and dissolved silica show (Sections 3.3.2 and 3.4.1), and adding dissolved silica as an extra variable did not change the four-factor solution.

The carbonate weathering factor accounts for most of the $HCO_3{}^-$ (72.75%), the bulk of the $Mg^{2+}$ (56.48%) and about a third of the $Ca^{2+}$ (28.45%). This is what the ion ratios and saturation indices already pointed to: the water is at or near equilibrium with calcite and dolomite, so the carbonate minerals control the $HCO_3{}^-$ and much of the hardness. The factor also carries 80.04% of the $F^-$. Because fluorite is $CaF_2$, its dissolution follows the calcium released by carbonate weathering, so a fluoride signal that rides on the carbonate factor is geochemically coherent; the very low $F^-$ concentrations and their proximity to the detection limit nevertheless prevent a separate fluorite source from being resolved.

The agricultural nitrogen factor supplies 95.62% of the $NO_3{}^-$ and therefore explains the nitrate pattern of the area, which matches the exceedance rate of 68.7%. It also accounts for 43.88% of the $Cl^-$, a common companion of farm and household waste. The sulfate mineral factor supplies 83.92% of the $SO_4{}^{2-}$ and 35.75% of the $Ca^{2+}$, and the halite–anthropogenic salt factor supplies 71.32% of the $Na^+$, 43.89% of the $Cl^-$ and 54.03% of the $K^+$.

Overall, the four factors contribute 36.85% (carbonate weathering), 27.41% (agricultural nitrogen), 24.81% (sulfate mineral dissolution) and 10.92% (halite–anthropogenic salt) of the solute mass (Figure 13). The bootstrap 5th–95th percentiles of these shares are 32.41–47.08%, 15.30–35.74%, 18.71–28.07% and 7.49–16.46%, so the ranking of the factors is stable even though the percentages themselves carry the usual uncertainty of a receptor model. Water–rock interaction, in the form of carbonate and sulfate mineral dissolution, is the leading control on the chemistry and carries about 62% of the solute mass. Human activity is the second control: agricultural nitrogen and salt input account for about 38%, and they are the only factors that can explain the nitrate and sodium chloride excess of the samples. Because the sulfate factor combines gypsum dissolution with possible sulfide oxidation from the coal measures, and the salt factor combines evaporite dissolution with anthropogenic salt, the boundary between the natural and human share is a range rather

than a sharp line. The data show that human inputs are a major, but not the dominant, contributor to the solute load of this karst water. The hydrochemical facies and the dominance of carbonate weathering found here agree with those reported for the other karst systems of central-southern Shandong [7,9,30,31], whereas the combined nitrate and sulfate pressure reflects the intensive farming and coal mining of the Zaozhuang basin; because the earlier studies differ in sampling design and period, this comparison remains qualitative.

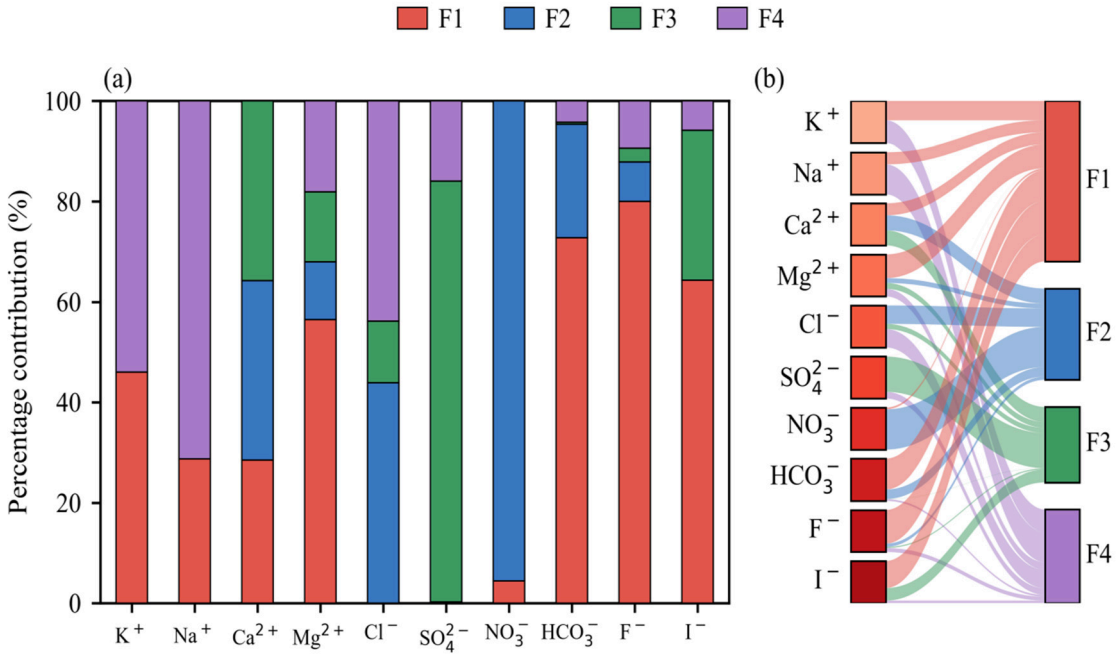



**Figure 13.** Contribution of the four PMF sources to each individual ion (**a**) and source-to-ion apportionment of the karst groundwater (**b**). F1: carbonate weathering; F2: agricultural nitrogen input; F3: sulfate mineral dissolution; F4: halite dissolution with anthropogenic salt input.

The four sources resolved here can be translated into management priorities. In the farming districts, where the agricultural nitrogen factor dominates, the priority is to reduce nitrate leaching: balanced fertiliser application, a shift of the application period away from the rainy season, better management of manure and domestic sewage in villages without sewerage, and protection of the karst fissures and dolines through which recharge reaches the aquifer rapidly. Where the halite–anthropogenic salt factor is concentrated, the priority is to control salt inputs, particularly sewage effluent and the storage and handling of industrial salt. The high-sulfate zones around the mining districts call for monitoring of mine drainage and coal waste piles. Because the present data set covers a single campaign, the most effective next step would be the routine monitoring network anticipated in the Introduction—a subset of the 131 points sampled in both the dry and the wet season for nitrate, sulfate, chloride and TDS—and the PMF solution can then be used to check the effectiveness of the measures over time.

Several limitations should be borne in mind. First, the 131 samples were collected in a single campaign (May 2025), so the results describe the spatial pattern of that period, and no seasonal or long-term trend can be derived from them; the comparison with the karst systems of Jinan and Tai'an is therefore qualitative. Second, nitrate is attributed to agriculture and human activity as a whole because the stable isotope data that would separate fertiliser from manure and sewage were not measured. Third, $F^-$ and $I^-$ lie close to their detection limits and are reproduced poorly by the model, so their shares are reported but are not used for source identification. Finally, the four PMF factors are statistical descriptions of covarying processes rather than physical end members, and the

natural and anthropogenic fractions of the sulfate and salt factors cannot be separated with the species measured here.

## 4. Conclusions

(1) The pH of the karst water ranges from 7.04 to 7.78 (mean 7.33, CV 2.13%), so the water is weakly alkaline and chemically stable. TDS ranges from 288 to 2578 mg/L (mean 609.10 mg/L), so the salinity is relatively high and clearly variable in space. $Ca^{2+}$ dominates the cations ($Ca^{2+} > Na^{+} > Mg^{2+} > K^{+}$) and $HCO_3^-$ the anions ($HCO_3^- > SO_4^{2-} > NO_3^- > Cl^-$), with the $HCO_3^-$Ca type prevailing. The ions vary distinctly in space: TDS, $Ca^{2+}$, $Mg^{2+}$ and $HCO_3^-$ are high in the east and low in the west, and they increase along the direction of groundwater flow.

(2) The water chemistry is controlled jointly by rock weathering and dissolution and anthropogenic inputs, whereas cation exchange modifies the ionic balance without adding solute mass. $Ca^{2+}$, $Mg^{2+}$, and $HCO_3^-$ are derived mainly from carbonate weathering and dissolution; $SO_4^{2-}$ mainly from the dissolution of sulfate minerals, including the oxidation of sulfide minerals in the coal measures; $Na^{+}$, $K^{+}$, and $Cl^-$ mainly from evaporite dissolution and anthropogenic inputs; and $NO_3^-$ mainly from agriculture. The ion ratios show that $Ca^{2+}$ and $SO_4^{2-}$ are strongly correlated and that sulfate minerals such as gypsum contribute clearly to the water chemistry. Samples with positive chloro-alkaline indices (CAI$^-$1 and CAI$^-$2) account for 71.0%, so cation exchange is dominated by the replacement of $Ca^{2+}$ and $Mg^{2+}$ by $Na^{+}$ and $K^{+}$ and is relatively strong. The Gibbs and end-member diagrams show that rock weathering and dissolution dominate the chemistry, with carbonate weathering foremost, while a contribution from evaporation cannot be excluded for a few high-TDS samples, although residence time and mixing are more plausible explanations in this sub-humid, monsoon-influenced karst setting.

(3) According to the saturation indices, calcite and aragonite are mostly in equilibrium or slightly oversaturated, dolomite is generally undersaturated and gypsum is clearly undersaturated, so carbonate dissolution has nearly reached equilibrium, whereas sulfate minerals such as gypsum continue to dissolve. Anthropogenic inputs clearly affect the karst water: nitrate exceeds the drinking water limit in 68.7% of the samples (90 of 131, against the maximum contaminant level of the United States Environmental Protection Agency of 10 mg/L nitrate as N; 57.3% of the samples exceed the WHO guideline value of 50 mg/L $NO_3^-$) and sulfate exceeds 250 mg/L—the limit of both GB 5749 and the WHO guidelines—in 12.98% of the samples (17 of 131). Agriculture is the leading human influence. Because the isotope data needed to separate fertiliser nitrogen from manure and sewage ($\delta^{15}$N-$NO_3^-$,$\delta^{18}$O-$NO_3^-$) were not measured, the nitrate is attributed to agricultural and anthropogenic sources without resolving its type.

(4) The PMF receptor model resolves four sources of the karst water chemistry: carbonate weathering, agricultural nitrogen input, sulfate mineral dissolution and halite dissolution with anthropogenic salt input. They carry 36.85%, 27.41%, 24.81% and 10.92% of the solute mass, with bootstrap 5th–95th percentiles of 32.41–47.08%, 15.30–35.74%, 18.71–28.07% and 7.49–16.46%. The model fits the measured concentrations with $Q/Q_{exp}$ = 1.17 and reproduces the eight major ions with a mean $R^2$ of 0.801. Carbonate weathering accounts for most of the $HCO_3^-$ and $Mg^{2+}$, the agricultural nitrogen factor accounts for 95.62% of the $NO_3^-$, sulfate mineral dissolution for 83.92% of the $SO_4^{2-}$ and the halite–anthropogenic salt factor for 71.32% of the $Na^{+}$ and 43.89% of the $Cl^-$. Carbonate and sulfate mineral dissolution together account for about 62% of the solute mass and remain the main control on the chemistry, while agricultural

nitrogen and salt input account for about 38% and are the main human contribution. The nitrogen sources are grouped as agricultural and anthropogenic.

**Author Contributions:** Conceptualization, B.L. and H.A.; methodology, B.L. and C.H.; software, B.L. and Z.W.; validation, Z.L., S.G. and Y.W.; formal analysis, B.L.; investigation, B.L., C.H., Z.L. and S.G.; resources, H.A. and B.J.; data curation, B.L. and K.L.; writing—original draft preparation, B.L.; writing—review and editing, B.L., Y.W. and H.A.; visualization, B.L. and Z.W.; supervision, H.A.; project administration, H.A.; funding acquisition, H.A. All authors have read and agreed to the published version of the manuscript.

**Funding:** This research was funded by the Natural Science Foundation of Shandong Province, grant number ZR2025MS568; the National Natural Science Foundation of China, grant number 42202294; and the China Geological Survey Project, grant number DD202605102003.

**Institutional Review Board Statement:** Not applicable

**Informed Consent Statement:** Not applicable

**Data Availability Statement:** The data presented in this study are available on request from the corresponding author.

**Conflicts of Interest:** The authors declare no conflict of interest.

## References

1. Wu, X.; Liu, H.; Liu, C.; Li, C.; Liu, J.; Geng, F.; Hu, X.; Kang, F. Mechanisms of water quantity and quality evolution in karst groundwater: New insights from long-term monitoring data. *J. Hydrol.* **2025**, *661*, 133634. [CrossRef]
2. Gao, S.; Li, C.; Liu, Y.; Sun, B.; Zhao, Z.; Lv, M.; Gang, S. Hydrogeochemical characteristics and evolution processes of karst groundwater affected by multiple influencing factors in a karst spring basin, eastern China. *Water* **2023**, *15*, 3899. [CrossRef]
3. Wang, R.; Li, X.; Wei, A. Hydrogeochemical characteristics and gradual changes of groundwater in the Baiquan karst spring region, northern China. *Carbonates Evaporites* **2022**, *37*, 47. [CrossRef]
4. Su, C.; Zhang, X.; Sun, Y.; Meng, S.; Cui, X.; Fei, Y. Hydrochemical characteristics and evolution processes of karst groundwater in Pingyin karst groundwater system, North China. *Environ. Earth Sci.* **2023**, *82*, 67. [CrossRef]
5. Liu, D.; Tian, C.; Chen, X.; Zhang, W.; Zhang, X.; Wang, Z.; Xu, D.; Chang, Y. Insights into karst groundwater hydrogeochemical characteristics and spatial evolution in the Jinan karst aquifer system, northern China. *Water Supply* **2023**, *23*, 5004–5016. [CrossRef]
6. Wang, Z.; Guo, X.; Kuang, Y.; Chen, Q.; Luo, M.; Zhou, H. Recharge sources and hydrogeochemical evolution of groundwater in a heterogeneous karst water system in Hubei Province, Central China. *Appl. Geochem.* **2022**, *136*, 105165. [CrossRef]
7. Zhang, Y.; Su, C.-L.; Ma, Y.-H.; Liu, W.-J. Indicators of groundwater evolution processes based on hydrochemistry and environmental isotopes: A case study of the Dongyuan drinking water source area in Ji'nan City. *Environ. Sci.* **2019**, *40*, 2667–2674.
8. Peng, Y.; Xiao, Q.; Xue, H.; Lv, M.; Lin, G.; Zhao, H.; Wu, P.; Guo, Y. Comparison of groundwater hydrogeochemistry of karst areas in northern and southern China with emphasis on their performance in karst development. *Carbonates Evaporites* **2022**, *37*, 69. [CrossRef]
9. Li, X.B.; Li, M.Y.; Zhang, X.M.; Ma, X.; Sun, D.; Meng, Q.; Ma, C. Source tracing of sulfate in a karst groundwater system in Tai'an City, Shandong Province. *Rock Mineral. Anal.* **2025**, *44*, 722–734.
10. Feng, Y.; Kang, F.; Guo, Y.; Li, Z.; Liu, B.; Bu, H.; Xia, C.; He, Q. Evolution of hydrochemistry and water quality of karst groundwater under the effects of intense anthropogenic activities. *J. Environ. Manag.* **2024**, *371*, 123059. [CrossRef] [PubMed]
11. Gibbs, R.J. Mechanisms controlling world water chemistry. *Science* **1970**, *170*, 1088–1090. [CrossRef] [PubMed]
12. Thurston, G.D.; Spengler, J.D. A quantitative assessment of source contributions to inhalable particulate matter pollution in metropolitan Boston. *Atmos. Environ.* **1985**, *19*, 9–25. [CrossRef]
13. Meng, L.; Zuo, R.; Wang, J.-S.; Yang, J.; Teng, Y.-G.; Shi, R.-T.; Zhai, Y.-Z. Apportionment and evolution of pollution sources in a typical riverside groundwater resource area using PCA-APCS-MLR model. *J. Contam. Hydrol.* **2018**, *218*, 70–83. [CrossRef] [PubMed]
14. Meng, L.; Zuo, R.; Wang, J.S.; Yang, J.; Teng, Y.G.; Zhai, Y.Z.; Shi, R.T. Quantitative source apportionment of groundwater pollution based on PCA-APCS-MLR. *China Environ. Sci.* **2017**, *37*, 3773–3786.
15. Zhang, H.; Cheng, S.; Li, H.; Fu, K.; Xu, Y. Groundwater pollution source identification and apportionment using PMF and PCA-APCA-MLR receptor models in a typical mixed land-use area in Southwestern China. *Sci. Total Environ.* **2020**, *741*, 140383. [CrossRef] [PubMed]

16. Hu, B.; Liu, Y.; Chen, Y.; Yao, Y.; Liu, H.; Wang, Z. Water quality and pollution source apportionment responses to rainfall in steppe lake estuaries: A case study of Hulun Lake in northern China. *Ecol. Indic.* **2024**, *168*, 112791. [CrossRef]
17. Zhou, Z.; Chen, M.; Li, Y. Source apportionment of groundwater contamination using integrated PCA-APCS-MLR modeling: A case study of an industrial zone in Southwest China. *Environ. Res.* **2026**, *292*, 123628. [CrossRef] [PubMed]
18. Ren, X.; Zhang, H.; Xie, G.; Hu, Y.; Tian, X.; Gao, D.; Guo, S.; Li, A.; Chen, S. New insights into pollution source analysis using receptor models in the upper Yangtze river basin: Effects of land use on source identification and apportionment. *Chemosphere* **2023**, *334*, 138967. [CrossRef] [PubMed]
19. Paatero, P.; Tapper, U. Positive matrix factorization: A non-negative factor model with optimal utilization of error estimates of data values. *Environmetrics* **1994**, *5*, 111–126. [CrossRef]
20. Norris, G.; Duvall, R.; Brown, S.; Bai, S. *EPA Positive Matrix Factorization (PMF) 5.0 Fundamentals and User Guide*; U.S. Environmental Protection Agency: Washington, DC, USA, 2014; EPA/600/R-14/108.
21. Paatero, P. Least squares formulation of robust non-negative factor analysis. *Chemom. Intell. Lab. Syst.* **1997**, *37*, 23–35. [CrossRef]
22. Zhang, C.; Zhang, B.; Zhang, W.; Zou, J.; Jia, R.; Yang, Y. Hydrochemical characteristics and evolution under the influence of multiple anthropogenic activities in karst aquifers, northern China. *Water* **2024**, *16*, 1656. [CrossRef]
23. Gong, W.; Zang, C.; Ma, J.; Sun, Y.; Zhang, H.; Xu, P.; Jiang, M. Hydrochemical characteristics and controlling factors of deep karst groundwater in Huaibei Plain, Huaihe River Basin, China. *Front. Earth Sci.* **2025**, *13*, 1552125. [CrossRef]
24. Deng, Q.; Wu, X.; Zhang, W.; Li, C.; Zhang, L.; Teng, Y.; Zhang, Y.; Li, G. Characteristics and source analysis of nitrate pollution of karst groundwater in the Xiaoli area of the lower Yellow River Basin. *Appl. Water Sci.* **2026**, *16*, 213. [CrossRef]
25. Mu, D.; Meng, J.; Wang, S.; Xiao, S.; Wang, H.; Sun, X.; Wu, P. Source apportionment, source-specific health risks, and control factors of heavy metals in water bodies of a typical karst basin in southwestern China. *PLoS ONE* **2024**, *19*, e0309142. [CrossRef] [PubMed]
26. Cheng, T.; Lu, H.; Qiao, X.; Zhang, Z.; Zhang, L.; Zhang, X.; Ding, Z.; Sun, N. Quantitative source apportionment of groundwater contamination in the Poyang Lake recharge area: Insights from PMF and PCA-APCS-MLR models. *Sustainability* **2026**, *18*, 7037. [CrossRef]
27. Wang, Q.; Gao, X.; Jiang, C.; Li, C.; Zhang, X.; Wang, W.; Duan, Y.; Luo, W.; Mao, Z.; Wang, Y. Multiple contamination sources, pathways and conceptual model of complex buried karst water system: Constrained by hydrogeochemistry and $\delta^{2}H$, $\delta^{18}O$, $\delta^{34}S$, $\delta^{13}C$ and $^{87}Sr/^{86}Sr$ isotopes. *J. Hydrol.* **2024**, *639*, 131614. [CrossRef]
28. Song, Y.S. Hydrochemical characteristics of the large karst springs in central-south Shandong Province. *Carsologica Sin.* **1992**, *11*, 29–37.
29. Xu, H.Z.; Li, W.P.; Yin, X.L.; Duan, X.; Gao, Z.; Wang, Q. Hydrochemistry and isotopes of shallow groundwater in the Jinan spring catchment. *Hydrogeol. Eng. Geol.* **2008**, *35*, 65–69.
30. Meng, L.H. Recharge source and evolution process of karst groundwater in Tai'an urban area based on hydrochemistry and hydrogen and oxygen isotopes. *Environ. Sci.* **2024**, *45*, 2096–2106.
31. Teng, Y.; Zhang, W.Q.; Wang, J.X. Analysis on hydrochemical characteristics and controlling factors of karst groundwater in Zihe River Basin. *Environ. Chem.* **2023**, *42*, 1945–1956.
32. Zhao, Q.L.; Li, Q.C.; Bu, H.; Wan, M. Hydrochemical characteristics and genesis of karst water in typical karst areas of central-southern Shandong: A case study of the Shuangcun karst water system. *J. China Hydrol.* **2015**, *35*, 70–76.
33. Paatero, P.; Hopke, P.K. Discarding or downweighting high-noise variables in factor analytic models. *Anal. Chim. Acta* **2003**, *490*, 277–289. [CrossRef]
34. Brown, S.G.; Eberly, S.; Paatero, P.; Norris, G.A. Methods for estimating uncertainty in PMF solutions: Examples with ambient air and water quality data and guidance on reporting PMF results. *Sci. Total Environ.* **2015**, *518–519*, 626–635. [CrossRef] [PubMed]
35. Parkhurst, D.L.; Appelo, C.A.J. *Description of Input and Examples for PHREEQC Version 3—A Computer Program for Speciation, Batch-Reaction, One-Dimensional Transport, and Inverse Geochemical Calculations*; U.S. Geological Survey: Reston, VA, USA, 2013; Techniques and Methods, Book 6, Chapter A43.
36. Tian, B.; Lu, C.; Zhao, D.; Li, J.; Zhu, H.; Dong, F. Hydrochemical evolution of karst groundwater and mining-induced activation effects in a coal mining area: A case study from the Tengxian coalfield, China. *ACS Omega* **2025**, *10*, 42548–42560. [CrossRef] [PubMed]
37. Xie, H.; Shen, H.-Y.; Zhang, H.-D.; Lin, Y.-S.; Li, J.; Liang, H.-Y.; Wang, Z.-H.; Zhu, T.-L.; Zou, S.-Z. Distributions and driving factors of hydrochemical compositions in different types of karst groundwater in Qingjiang River Basin. *Environ. Sci.* **2025**, *46*, 1417–1426. [CrossRef] [PubMed]
38. Huang, Q.-B.; Qin, X.-Q.; Cheng, R.-R.; Li, T.-F.; Wu, H.-Y.; Liao, H.-W. Investigation of the hydrogeochemical processes and regional evolution of karst groundwater in Liulin Spring catchment, northern China. *Environ. Earth Sci.* **2021**, *80*, 20. [CrossRef]
39. Zhang, C.; Li, X.; Wang, Z.; Hou, X.; Ma, J.; Gao, M.; Bai, Z.; Fu, C.; Gui, C.; Zuo, X. Combining stable isotope ($^{2}H$, $^{18}O$, and $^{87}Sr/^{86}Sr$) and hydrochemistry to understand hydrogeochemical processes in karst groundwater system, Xin'an, northern China. *Environ. Earth Sci.* **2023**, *82*, 224. [CrossRef]

40. Li, C.; Gui, H.; Guo, Y.; Chen, J.; Li, J.; Xu, J.; Yu, H. Study on the influence of mining activities on the quality of deep karst groundwater based on multivariate statistical analysis and hydrochemical analysis. *Int. J. Environ. Res. Public Health* **2022**, *19*, 17042. [CrossRef] [PubMed]
41. Zhu, X.; Liu, L.; Lan, F.; Li, J.; Hou, S. Hydrogeochemistry characteristics of groundwater in the Nandong karst water system, China. *Atmosphere* **2022**, *13*, 604. [CrossRef]
42. Hou, Q.; Pan, Y.; Zeng, M.; Wang, S.; Shi, H.; Huang, C.; Peng, H. Assessment of groundwater hydrochemistry, water quality, and health risk in Hainan Island, China. *Sci. Rep.* **2023**, *13*, 12104. [CrossRef] [PubMed]
43. Ma, Q.; Ge, W.; Tian, F. Geochemical characteristics and controlling factors of chemical composition of groundwater in a part of the Nanchang section of Ganfu Plain. *Sustainability* **2022**, *14*, 7976. [CrossRef]
44. Liu, L.; Lan, J.; Ren, K.; Huang, M.; Mao, R.; Zhang, X.; Yue, K. Enhanced carbonate weathering and $CO_2$ release in a typical karst watershed (Southwest China): Evidence from hydrochemical and multi-isotopic data. *Sci. Total Environ.* **2024**, *957*, 177372. [CrossRef] [PubMed]
45. Asmoay, A.A.; Mabrouk, W.A. Appraisal of rock-water interaction and frailty of groundwater to corrosion and salinization, northwestern Gulf of Suez, Egypt. *J. Umm Al-Qura Univ. Appl. Sci.* **2024**, *10*, 39–50. [CrossRef]
46. Zhu, M.; Chen, J.; He, C.; Ren, S.; Liu, G. Multi-method characterization of groundwater nitrate and sulfate contamination by karst mines in southwest China. *Sci. Total Environ.* **2024**, *946*, 174375. [CrossRef] [PubMed]
47. Ye, H.; Han, Z.; Wu, P.; Zha, X.; Li, X.; Hou, E.; Cao, Y.; Tang, C.; Zhang, R.; Sardans, J.; et al. Disentangling sources and transformation mechanisms of nitrogen, sulfate, and carbon in water of a karst critical zone. *Sci. Total Environ.* **2024**, *922*, 171310. [CrossRef] [PubMed]
48. Shi, J.; Jiang, G.; Guo, F.; Sun, Z.; Liu, F. Hydrogeological controls and anthropogenic impacts on groundwater dissolved organic matter in karst aquifers: A comparison of peak-cluster depression and peak-forest plain systems. *J. Hydrol.* **2026**, *667*, 134805. [CrossRef]
49. Lu, D.; Chen, J.P.; Yan, Y.; Yang, X.; Liu, C.; Geng, Z. Hydrochemical characteristics and source contribution analysis of pore water in Beichuan River Basin, Qinghai Province. *Geol. Rev.* **2025**, *71*, 233–244.


**Disclaimer/Publisher's Note:** The statements, opinions and data contained in all publications are solely those of the individual author(s) and contributor(s) and not of MDPI and/or the editor(s). MDPI and/or the editor(s) disclaim responsibility for any injury to people or property resulting from any ideas, methods, instructions or products referred to in the content.